



Hemodynamic assessment of pulmonary hypertension in mice: a model-based analysis of the disease mechanism

M. Umar Qureshi¹ · Mitchel J. Colebank¹ · L. Mihaela Paun² · Laura Ellwein Fix³ · Naomi Chesler⁴ · Mansoor A. Haider¹ · Nicholas A. Hill² · Dirk Husmeier² · Mette S. Olufsen¹

Received: 16 March 2018 / Accepted: 17 September 2018
© Springer-Verlag GmbH Germany, part of Springer Nature 2018

Abstract

This study uses a one-dimensional fluid dynamics arterial network model to infer changes in hemodynamic quantities associated with pulmonary hypertension in mice. Data for this study include blood flow and pressure measurements from the main pulmonary artery for 7 control mice with normal pulmonary function and 5 mice with hypoxia-induced pulmonary hypertension. Arterial dimensions for a 21-vessel network are extracted from micro-CT images of lungs from a representative control and hypertensive mouse. Each vessel is represented by its length and radius. Fluid dynamic computations are done assuming that the flow is Newtonian, viscous, laminar, and has no swirl. The system of equations is closed by a constitutive equation relating pressure and area, using a linear model derived from stress–strain deformation in the circumferential direction assuming that the arterial walls are thin, and also an empirical nonlinear model. For each dataset, an inflow waveform is extracted from the data, and nominal parameters specifying the outflow boundary conditions are computed from mean values and characteristic timescales extracted from the data. The model is calibrated for each mouse by estimating parameters that minimize the least squares error between measured and computed waveforms. Optimized parameters are compared across the control and the hypertensive groups to characterize vascular remodeling with disease. Results show that pulmonary hypertension is associated with stiffer and less compliant proximal and distal vasculature with augmented wave reflections, and that elastic nonlinearities are insignificant in the hypertensive animal.

Keywords Pulmonary hypertension · 1D fluid dynamics model · Linear and nonlinear wall model · Parameter estimation · Statistical model selection · Wave intensity analysis · Impedance analysis

Electronic supplementary material The online version of this article (<https://doi.org/10.1007/s10237-018-1078-8>) contains supplementary material, which is available to authorized users.

✉ Mette S. Olufsen
msolufse@ncsu.edu

M. Umar Qureshi
muquresh@ncsu.edu

Mitchel J. Colebank
mjcoleba@ncsu.edu

L. Mihaela Paun
l.paun.1@research.gla.ac.uk

Laura Ellwein Fix
lellwein@vcu.edu

Naomi Chesler
naomi.chesler@wisc.edu

Mansoor A. Haider
m_haider@ncsu.edu

1 Introduction

Pulmonary hypertension (PH) is defined as an invasively measured mean pulmonary arterial blood pressure (mPAP)

Nicholas A. Hill
nicholas.hill@glasgow.ac.uk

Dirk Husmeier
dirk.husmeier@glasgow.ac.uk

¹ Department of Mathematics, North Carolina State University, Raleigh, NC 27695, USA

² School of Mathematics and Statistics, University of Glasgow, Glasgow G12 8QQ, UK

³ Department of Mathematics and Applied Mathematics, Virginia Commonwealth University, Richmond, VA 23284, USA

⁴ Department of Biomedical Engineering, University of Wisconsin-Madison, Madison, WI 53706, USA

greater than 25 mmHg (Simonneau et al. 2013). It is associated with vascular remodeling, which adversely affects the properties of the cardiopulmonary system, including pulmonary vascular resistance (PVR), proximal and distal arterial stiffness, compliance, and amplitude of wave reflections (Nichols et al. 2011). The mPAP and PVR are conventionally used diagnostic markers for PH but are not good indicators of disease severity (Wang and Chesler 2011). Here we use proximal arterial stiffness and the wave reflection amplitude as physiomarkers for detecting disease progression (Castelain et al. 2001; Hunter et al. 2011). In particular, the proximal arterial stiffness is an excellent predictor of mortality in patients with pulmonary arterial hypertension (Gan et al. 2007). Quantifying relative distributions of proximal and distal arterial stiffness (or compliance) and wave reflections in elevating the mPAP and PVR is vital for understanding disease mechanisms.

In this study, we setup and calibrate a mathematical model predicting wave propagation in the pulmonary vasculature in C57BL6/J male mice with normal pulmonary function [control group (CTL), $n = 7$] and in mice with hypoxia-induced pulmonary hypertension [hypertensive group (HPH), $n = 5$] (Tabima et al. 2012; Vanderpool et al. 2011). The novelty of this study is the integration of high fidelity morphometric and hemodynamic data from multiple mice with a one-dimensional (1D) model of large pulmonary arteries coupled with a zero-dimensional (0D) model of the vascular beds. This is achieved by incorporating available data at each stage of the modeling including network extraction, parameter estimation and model validation. The outcome is used to infer disease progression by quantifying relative changes in PVR, proximal and distal arterial stiffness, compliance, and amplitudes of wave reflections, across the two groups (CTL and HPH). Moreover, we investigate the influence of presumed elastic nonlinearities in the wall model on the parameter inference. This approach allows us to study disease impact on the distal vasculature by predicting waveforms from multiple locations in the simulated network, which are difficult to obtain experimentally.

1.1 Experimental studies

To understand the relation between hemodynamics and vascular remodeling, it is essential to analyze morphometric and hemodynamic time-series data during disease progression. Morphometric data can be obtained by noninvasive procedures, like magnetic resonance imaging (MRI) or computed tomography (CT) scans (Meaney and Beddy 2012), but dynamic pulmonary blood pressure can only be obtained from right heart catheterization (Rich et al. 2011). Moreover, in humans, the disease takes years to develop making it difficult to study its progression. An alternative means to gain understanding is to study disease progression in mouse

models. An advantage is that mice have a relatively short life span and it is feasible to generate specific disease groups (e.g. mice with HPH) within a short time-span (< 1 month). Experimental studies in mice are typically done within a specific genetic strain, in order to limit variation among individuals. In most studies [e.g. Pursell et al. (2016), Tabima et al. (2012) and Vanderpool et al. (2011)], hypoxia is used to induce pulmonary hypertension. This type of PH (Group III) is clinically manifested in human patients with hypoxia and lung disease (Simonneau et al. 2013), believed to be initiated by remodeling of the vascular beds [e.g. microvascular vasoconstriction and rarefaction (Wang and Chesler 2011)] followed by progressive remodeling of the large arteries (Tuder et al. 2007). Therefore, investigation of pulmonary hypertension in mice with hypoxia may provide vital understanding of disease mechanisms in humans with similar pathology.

1.2 Modeling studies

Examples of previous modeling efforts include lumped 0D (Lankhaar et al. 2006; Lumens et al. 2009), distributed 1D (Acosta et al. 2017; Lungu et al. 2014; Qureshi et al. 2014) and locally complex three-dimensional (3D) (Tang et al. 2012; Yang et al. 2016) models. Lankhaar et al. (2006) combined a 0D 3-element Windkessel model with hemodynamic data from PH patients to quantify right ventricular afterload. Lumens et al. (2009) developed a geometric heart model coupled with a closed loop 0D model of the entire circulation to predict ventricular hypertrophy in patients with PH. Tang et al. (2012) and Yang et al. (2016) constructed patient-specific 3D models of pulmonary arteries to study shear stress (Tang et al. 2012), and PVR in pre- and postoperative situations (Yang et al. 2016). To our knowledge, only Lungu et al. (2014) used a coupled 1D–0D model of the main pulmonary artery (MPA) to study diagnostic parameters including PVR, mPAP, arterial stiffness and compliance in patients with and without PH. Studies by Acosta et al. (2017) and Qureshi et al. (2014) used a 1D framework to develop distributed models of the pulmonary arteries and veins to study cardiopulmonary coupling (Acosta et al. 2017) and microvascular remodeling (Qureshi et al. 2014) during PH. Yet, none of these studies used actual pressure data for parameter estimation and model validation. Other notable studies using 1D models, but not investigating pulmonary hypertension, include Blanco et al. (2014), Mynard and Smolich (2015), Olufsen et al. (2000), Reymond et al. (2009) and Willemet and Alastruey (2015). See Boileau et al. (2015), Safaei et al. (2016) and van de Vosse and Stergiopoulos (2011) for an overview of modeling approaches and computational tools, and Hunter et al. (2011), Kheyfets et al. (2013) and Tawhai et al. (2011) for focused reviews on modeling pulmonary hypertension.

Most of the above studies consider application to humans. Only a few of 1D modeling studies have investigated wave

propagation in systemic (Aslanidou et al. 2016) and pulmonary (Lee et al. 2016; Qureshi et al. 2017) arteries in mouse networks. To our knowledge, no studies combine disease-specific imaging and hemodynamics data to predict changes in disease. In this study, we expand upon prior results from Qureshi et al. (2017) by developing a 1D fluid dynamics network model of pulse wave propagation in the large pulmonary arteries of control and hypertensive mice. We do so by extracting detailed network information and by optimizing hemodynamic predictions. To set up the 1D domain, we extract the arterial networks from micro-CT images of a representative CTL mouse and a mouse with HPH. We combine these networks with hemodynamic data, measured in the MPA of each mouse, to predict pressure and flow waveforms. For each vessel in the network, we solve (numerically) fluid dynamics equations derived from the Navier–Stokes equations coupled with a constitutive equation relating pressure and vessel area (i.e. describing the vessel wall mechanics). We use the measured flow waveform from each mouse as the inflow boundary condition and use 0D Windkessel models (Westerhof et al. 2009) to characterize the impedance of the vascular beds.

As the disease progresses, vascular remodeling changes the composition of wall constituents (Humphrey 2008). This affects the local stress–strain response, which is important for inferring arterial wall stiffness and compliance (Hunter et al. 2011). We focus on understanding how wall deformation changes under hypertensive conditions. Specifically, we aim to study if presumed elastic nonlinearities have a significant impact on disease progression. To this end, we use a well-established linear wall model (Willemet and Alastruey 2015; Safaei et al. 2016) as well as an empirical nonlinear wall model.

The advantage of the linear wall model is that it is easy to derive from first principles and it has been shown to be successful within physiological pressure/area ranges for systemic arteries (Olufsen et al. 2000). Yet, it does not account for the fact that arteries stiffen with pressure. On the other hand, detailed, structural hyperelastic wall models can be derived from first principles, e.g. Holzapfel and Ogden (2010), but they are difficult to analyze due to the large number of parameters. Inspired by Langewouters et al. (1985), we introduce a simple empirical nonlinear model with three key properties: (a) it predicts vessel stiffening with pressure so that the lumen area approaches a finite limit as pressure increases, (b) it incorporates an undeformed area (or radius) corresponding to zero transmural pressure, and (c) it reduces to the linear wall model under a small strain assumption providing a basis for model comparison and nominal parameter estimation.

The process of modeling requires a priori specification of parameters, including proximal arterial stiffness, total vascular resistance, and peripheral compliance, which are known

to vary across individuals. This creates the need for methods to estimate parameters that predict observed hemodynamics across individual mice. A few recent studies have performed parameter estimation in blood flow models, including the study by Eck et al. (2017), which used polynomial chaos expansion to analyze a stochastic model of pressure waves in the large systemic arteries, the study by Arnold et al. (2017), which used an ensemble Kalman filter (EnKF) to estimate the unknown inflow to a single vessel, representing the ovine aorta, and the study by Tran et al. (2017), which used a Bayesian Markov chain Monte Carlo (MCMC) approach to estimate parameters in a multi-scale three-dimensional model of coronary arteries. Similarly, in the recent study by Paun et al. (2018), we used MCMC to estimate parameters for a 1D model of mouse pulmonary arteries. It should be noted that MCMC algorithms come at a substantial computational cost, making them infeasible for multi-subject studies. Other studies estimating pressure dynamics using optimization algorithms were done using either 0D (Valdez-Jasso et al. 2011; Williams et al. 2014) or 1D (Lungu et al. 2014) models. Yet, none of these studies investigated hemodynamic variation in the pulmonary arterial network.

In this study, we estimate global network parameters that allow prediction of observed dynamics in both CTL and HPH groups. We first determine a priori parameter values for the wall models and boundary conditions. This is done by combining available data and existing results in the literature (Alastruey et al. 2016; Reymond et al. 2009). Second, we solve the overall model using linear and nonlinear wall models and conduct constrained nonlinear optimization to estimate parameters predicting the observed dynamics. A similar approach combining a priori nominal parameters with iterative tuning was used by Alastruey et al. (2016) in a model of the human aorta. In this study, blood flow data were available for all terminal vessels, making it easier to compute downstream resistance. To our knowledge, our approach estimating parameters for a 1D network model of the pulmonary circulation using morphometric and dynamic pressure and flow data is novel relative to these studies.

Similar to previous studies (Lee et al. 2016; Qureshi et al. 2014, 2017), we compare the hemodynamic signatures in the time and frequency domains for the control and hypertensive animals. We follow Acosta et al. (2017), Lankhaar et al. (2006) and Lungu et al. (2014) to analyze the estimated parameters, inferring HPH progression, and to investigate, using a model selection criterion (Burnham and Anderson 2002; Schwarz 1978), the extent to which the nonlinear wall model enables accurate prediction of the observed dynamics.

The manuscript is organized as follows: Sect. 2 presents experimental and mathematical methods including data extraction procedures, governing equations, parameter estimation and numerical simulations. In Sect. 3, we present results comparing CTL and HPH hemodynamics, analyzing:

waveforms predictions along the arterial network, estimated parameters and their sensitivities to hypertensive conditions, impedance and wave reflections. Key findings are discussed in Sect. 4, followed by limitations in Sect. 4.4. Finally, we state key conclusions in Sect. 5.

2 Methods

2.1 Experimental methods

This study uses existing hemodynamic data and micro-computed tomography (micro-CT) images from control and hypertensive mice. Detailed experimental protocols for extracting the hemodynamic and image data can be found in Tabima et al. (2012) and Vanderpool et al. (2011), respectively. Both procedures were approved by the University of Wisconsin Institutional Animal Care and Use Committee. Below we summarize these protocols and highlight the data analyzed herein.

2.1.1 Hemodynamic data

The hemodynamic data include dynamic pressure and flow waveforms from male C57BL6/J mice, average age 12–13 weeks and average body weight of 24 g. The mice were divided into CTL ($n = 7$) and HPH groups ($n = 5$). The mice in the HPH group were exposed to 21 days of chronic hypoxia (10% O₂ partial pressure) and both groups were exposed to a 12-h light–dark cycle. Mice were instrumented to obtain dynamic pressure and flow waveforms in the main pulmonary artery as described and validated previously by Tabima et al. (2012) and Schreier et al. (2014). In brief, mice were anesthetized with an intraperitoneal injection of urethane solution (2 mg/g body weight) and placed on a heating pad to maintain physiological heart rate. After intubation for ventilation, the chest wall was removed to expose the right ventricle. A 1.0 F pressure-tip catheter (Millar Instruments, Houston, TX) was inserted into the apex of right ventricle and advanced to the MPA. The stabilized pressure contour was recorded at 5 KHz on a hemodynamic work station (Cardiovascular Engineering, Norwood, MA, USA). Flow was measured with ultrasound (Visualsonics, Toronto, Ontario, Canada) using a 40 MHz probe during catheterization and recorded, processed and analyzed synchronously with pressure and ECG on the same custom made workstation. Flow velocity was calculated by velocity time integral using spectral analysis of the digitized broadband Doppler audio signal obtained in the proximal main pulmonary artery with the probe in a right parasternal long-axis orientation in the same location as the catheter. Measurement at this location allows for a better detection of MPA inner diameter, needed for calculation of volume flow rate from the flow velocity. The probe

was angled until the maximal velocity signal was obtained. A signal averaged flow velocity waveform was then obtained by tracing the spectral envelop. Measurement of the MPA inner diameter was taken using the long-axis view from leading edge to leading edge in B-mode imaging during the end systole and averaged from three cardiac cycles. MPA inner diameter was used to convert the instantaneous flow velocity to instantaneous volume flow rate (q) assuming a flat velocity profile across the circular cross section. Pressure and flow waveforms were aligned and signal-averaged using the ECG as a fiducial point. Twenty consecutive cardiac cycles were averaged to produce average pressure and average flow waveforms.

Representative hemodynamic data and associated frequency domain signatures are shown in Fig. 1 and essential cardiovascular parameters are summarized in Table 1. We

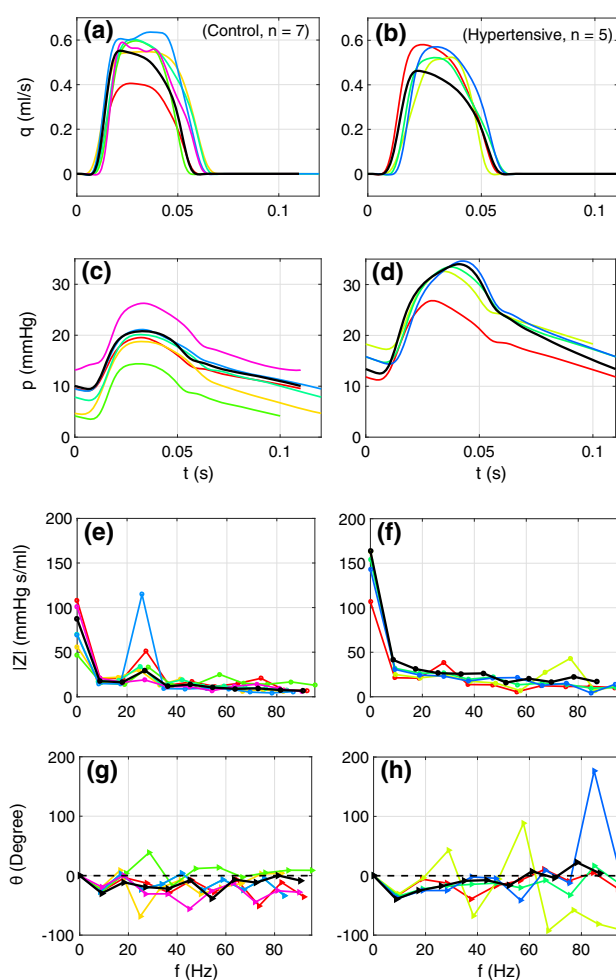


Fig. 1 **a–d** Simultaneously measured flow and pressure waveforms in MPA of control and hypertensive mice. Each waveform is averaged over 20 consecutive cardiac cycles. **e–h** Show associated frequency domain signatures, where f is the frequency, $|Z|$ is impedance modulus and θ is the associated phase angle [see Eq. (20)]. Thick black curves represent the representative control and hypertensive animal for which simulations are presented in this study

Table 1 Average hemodynamic characteristics (mean \pm SD) for the control and hypertensive animals

	CTL ($n = 7$)	HPH ($n = 5$)
HR (beats/min) [†]	533 \pm 27	559 \pm 21
CO (ml/s)*	0.18 \pm 0.03	0.15 \pm 0.01
mPAP (mmHg)	13.4 \pm 3.1	22.1 \pm 2.3
sPAP (mmHg)	20.1 \pm 3.5	32.3 \pm 3.1
dPAP (mmHg)	8.0 \pm 3.3	14.0 \pm 2.3
pPAP (mmHg)	12.2 \pm 1.4	18.3 \pm 2.8
PVR (mmHg.s/ml)	77.0 \pm 22.7	146.1 \pm 23.6

Heart rate (HR), cardiac output (CO), mean pressure (mPAP), systolic pressure (sPAP), diastolic pressure (dPAP), pulse pressure (pPAP) in the main pulmonary artery, total pulmonary vascular resistance (PVR)

[†] $P = 0.03$; *Change due to HPH is insignificant ($P > 0.05$); $P < 0.01$ for all other parameters

used the unpaired two-sample t test in MATLAB (*ttest2*) with a 95% confidence interval to compare quantities between the two groups. In the hypertensive mice, we found that the heart rate (HR), main pulmonary artery mean (mPAP), systolic (sPAP), diastolic (dPAP), and pulse pressure (pPAP), as well as total pulmonary vascular resistance (PVR) were significant ($P < 0.05$), while the decrease in cardiac output (CO) was statistically insignificant, $P > 0.05$ respectively. Moreover, it can be noted from Fig. 1c (the magenta curve), and Fig. 1d (the red curve) that there is a borderline animal in each group but none of them can be classified as a clear outlier. It is possible that a CTL mouse is mildly hypertensive and that one of the HPH mice is more resilient to the hypoxic conditions. Such animals were retained in our analysis to represent a more realistic population sample.

2.1.2 Imaging data

Stacked planar X-ray micro-CT images of pulmonary arterial trees were obtained from male C57BL6/J mice, average age 10–12 weeks, under control (healthy mice) and 10 days of hypobaric hypoxia at 10% O₂ partial pressure protocols. Detailed descriptions of animal handling and lung preparation can be found in Vanderpool et al. (2011), whereas details of the micro-CT image acquisition are described in Karau et al. (2011). In brief, mice were anesthetized with intraperitoneal injection of pentobarbital sodium (52 mg/kg body weight) and then euthanized by exsanguination. The trachea and the main pulmonary artery were cannulated, and the heart was dissected away. Pulmonary artery cannula (PE-90 tubing, 1.27 mm external and 0.86 mm internal diameter) was positioned well above the first bifurcation. Excised lungs were treated with Rho kinase inhibitor and ventilated and perfused with perfluorooctyl bromide (PFOB), a vascular contrast agent, and placed in the imaging chamber. The arterial trees were then imaged under a static filling pressure of

6.3 mmHg, while rotating the lungs in the X-ray beam at 1° increments to obtain 360 planar images. Each planar image was averaged over seven frames to minimize noise and maximize vascular contrast. The spatial resolution of volumetric lung scans were between 30 and 40 μ m. For each lung, isometric 3D volumetric dataset ($497 \times 497 \times 497$ pixels) was obtained, by reconstructing the 360 planar images using the Feldkamp cone-beam algorithm (Feldkamp et al. 1984), and converted into Dicom 3.0.

For this study, two representative networks with 21 vessels were extracted from images of the control and hypertensive mice. The 21-vessel network was chosen since it was the most expansive network that could be identified with a one-to-one vessel map in both control and hypertensive animals. Network dimensions and connectivities were obtained using the segmentation protocol described by Ellwein et al. (2016). This protocol uses ITK-SNAP (Yushkevich et al. 2006) to create a 3D geometry from Dicom 3.0 files, using semi-automated “snake evolution” in the regions of interest (the 21 vessels). To distinguish the foreground (vasculature) from the background (all other parts of the image), image voxels must be converted from their grayscale intensity values, ranging between 0 and 255, to a binary map. ITK-SNAP provides a voxel mapping function, which requires a lower and upper threshold separating the foreground from the background, as well as a smoothness parameter, which determines the slope of the mapping function. The imaging data used here are from an excised lung vasculature, eliminating the need for an upper voxel intensity bound. To minimize artifact detection, the lower threshold was set at 45 as all voxels in the vessels had intensities above this value. The default smoothness value 3.0 was used for simplicity. Paraview (Kitware; Clifton Park, NY) was used to convert file types to vtk polygonal data (.vtp) allowing us to compute centerlines and connectivity using the Vascular Modeling ToolKit [VMTK (Antiga et al. 2008)]. The output from VMTK is a $n \times 4$ matrix representing each vessel by a unique set of coordinates $\mathbf{x}_i \in \mathbb{R}^3$ ($i = 0, \dots, n - 1$) and the associated radius value, r_i , computed from the maximally inscribed sphere within the 3D vessel. Known internal diameter of the contrast filled cannula (PE-90 tubing) was used to compute a scaling factor to convert voxels into cm. For the MPA, the radius \bar{r}_0 was computed as a mean of all slices r_i between the cannulated region and the first bifurcation, whereas the radii of other vessels were computed as the mean of all slices along the vessels but away from the junctions. For each vessel, the length, L , was calculated as the sum of the shortest distances (l_i) between successive points, i.e.

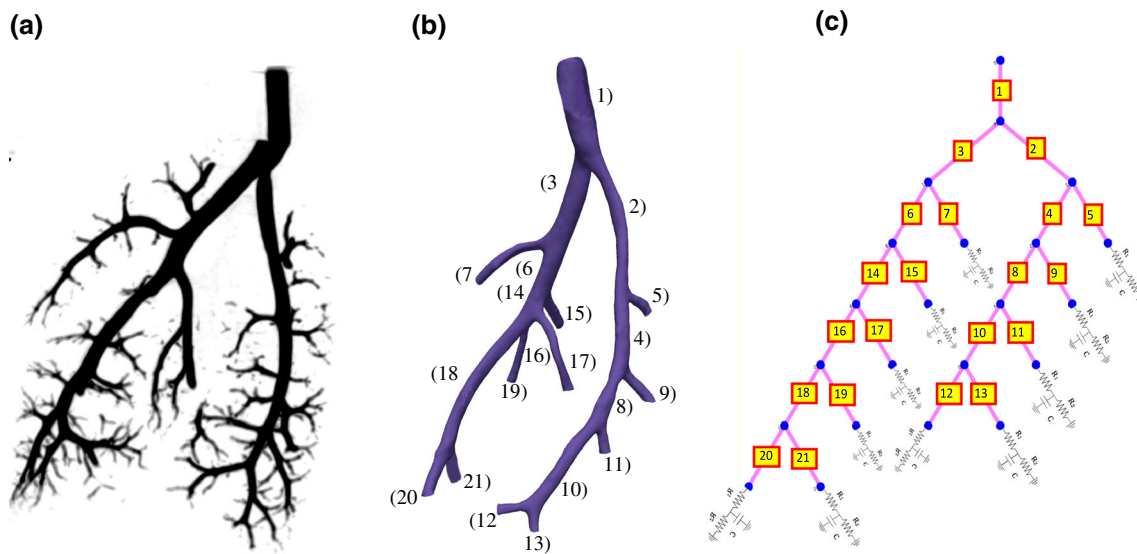


Fig. 2 1D network segmentation: **a** the micro-CT image, **b** 3D smoothed network for centerline extraction, and **c** the directed graph reflecting connectivity of vessels in the network. The size of segments in the graph do not reflect their dimensions

$$\bar{r}_0 = \frac{1}{n} \sum_i r_i, \quad L = \sum_i l_i, \quad \text{where } l_i = \|\mathbf{x}_{i+1} - \mathbf{x}_i\|, \quad (1)$$

$$\frac{\partial A}{\partial t} + \frac{\partial q}{\partial x} = 0, \quad \frac{\partial q}{\partial t} + \frac{\partial}{\partial x} \left(\frac{q^2}{A} \right) + \frac{A}{\rho} \frac{\partial p}{\partial x} = - \frac{2\pi \nu r}{\delta} \frac{q}{A}, \quad (2)$$

$i = 0, \dots, n-1$ and n is the total number of samples for the vessel. The network, in its load free state (i.e. at zero transmural pressure) is then constructed by assigning L and $r_0 = \bar{r}_0$ to each vessel. The shared coordinates information is used to generate a connectivity map of the 3D structure (see Fig. 2c) using the *digraph* function in MATLAB (version 16a). Both control and hypertensive networks have the same connectivity illustrated in Fig. 2c, but the individual vessel radii and length vary as shown in Table 2.

Finally, while it is known that the largest pulmonary arteries in humans taper along their lengths (Qureshi et al. 2014), analysis of imaging data from mouse pulmonary arteries did not allow us to determine taper within individual vessel segments. In general, pulmonary vasculature bifurcates quicker, making it harder to determine the tapering in individual vessels. However, improvements in segmentation methods can allow better quantification of tapering. Nevertheless, even in mice, the main pathways visibly taper in an exponential fashion. To avoid fitting a specific curve along data that has to be matched at each bifurcation, we chose to include actual mean radius measurements for each vessel to naturally account for tapering pathways.

2.2 Fluid dynamics model

Assuming that blood is incompressible, flow is Newtonian, laminar and axisymmetric, and has no swirl, conservation of mass and momentum (Olufsen et al. 2000) are given by

where x and t are the axial and temporal coordinates, $p(x, t) = p_{in}(x, t) - p_{ex}$ (mmHg) is the transmural blood pressure, p_{in} and p_{ex} are the pressures acting in and outside the arterial wall, respectively, $q(x, t)$ (ml/s) is the volumetric flow rate, $A(x, t) = \pi r^2$ (cm²) is the cross-sectional area and $r(x, t)$ (cm) is the vessel radius. The blood density ρ (g/ml) and the kinematic viscosity ν (cm²/s) are assumed constant. The momentum equation is derived under the no-slip condition assuming that the wall is impermeable, and that the velocity of the fluid at the wall equals the velocity of the wall. To satisfy this condition, we assume that the velocity profile over the lumen area is flat, decreasing linearly within the boundary layer with thickness $\delta = \sqrt{\nu T / 2\pi}$ (van de Vosse and Stergiopulos 2011).

2.3 Wall model

To close the system of equations, a constitutive equation relating pressure and cross-sectional area is needed. In this study, we compare two models. A linear elastic model (Safaei et al. 2016) derived from balancing circumferential stress and strain, and an empirical nonlinear wall model inspired by Langewouters et al. (1985).

The linear wall model is derived under the assumptions that the vessels are cylindrical and purely elastic, that the walls are thin ($h/r_0 \ll 1$), incompressible and homogeneous, that the loading and deformation are axisymmetric, and that the vessels are tethered in the longitudinal direction. Under these

Table 2 Dimensions of vessels in the 21-vessel network

Vessel index	Connectivity (daughters)	Control		Hypertensive	
		$r_0 \times 10^{-1}$ (cm)	$L \times 10^{-1}$ (cm)	$r_0 \times 10^{-1}$ (cm)	$L \times 10^{-1}$ (cm)
1 ^a	(2,3)	0.47	4.10	0.51	3.58
2	(4,5)	0.26	4.45	0.26	4.03
3	(6,7)	0.37	3.72	0.37	3.08
4	(8,9)	0.24	2.41	0.25	2.92
5	–	0.13	0.52	0.17	0.65
6	(14,15)	0.32	2.02	0.28	1.60
7	–	0.17	2.12	0.19	0.93
8	(10,11)	0.23	3.11	0.24	2.06
9	–	0.17	1.77	0.17	0.51
10	(12,13)	0.20	2.62	0.22	2.37
11	–	0.16	0.69	0.17	0.88
12	–	0.15	1.40	0.19	1.27
13	–	0.14	0.62	0.15	0.51
14	(16,17)	0.26	0.81	0.27	1.20
15	–	0.19	1.84	0.19	1.55
16	(18,19)	0.25	0.83	0.26	0.71
17	–	0.15	3.02	0.18	1.68
18	(20,21)	0.24	4.69	0.24	3.55
19	–	0.15	1.77	0.18	1.86
20	–	0.22	1.78	0.23	2.24
21	–	0.18	0.55	0.19	1.07

^aRoot vessel. Connectivity (i, j), i denotes the left daughter and j the right daughter. Vessels indicated by – are terminal

conditions, the external forces can be reduced to stresses in the circumferential direction, and Laplace's law (Nichols et al. 2011) gives a linear stress–strain relation

$$p = \beta \left(\sqrt{\frac{A}{A_0}} - 1 \right), \quad \text{where } \beta = \frac{Eh}{(1 - \kappa^2)r_0} \quad (3)$$

is the stiffness parameter, defined in terms of Young's modulus E in the circumferential direction. The associated Poisson ratio is κ , the wall thickness is h , and the undeformed radius is r_0 at zero transmural pressure ($p = 0$). $A_0 = \pi r_0^2$ (cm²) denotes the undeformed cross-sectional area. Similar to previous studies [e.g. Olufsen et al. (2000) and Safaei et al. (2016)], we use $\kappa = 0.5$.

The nonlinear wall model relates pressure and area as

$$p = p_1 \tan \left[\frac{\pi}{\gamma} \left(\frac{A}{A_0} - 1 \right) \right], \quad (4)$$

where $p_1 > 0$ (mmHg) is a material parameter that describes the half width pressure, and $\gamma > 0$ is a scaling parameter that determines the maximal lumen area A_∞ as $p \rightarrow \infty$, giving

$$A_\infty = (1 + \gamma/2)A_0. \quad (5)$$

This model is formulated to ensure that $A = A_0$ at $p = 0$.

2.4 Boundary conditions

Since the system of equations is hyperbolic, boundary conditions must be specified at the inlet and outlet of each vessel, i.e. the network needs an inflow condition, junction conditions, and outflow conditions.

At the network inlet, we specify a flow waveform extracted from hemodynamic data (see Fig. 1). At junctions (all bifurcations in the network studied), we impose pressure continuity and conservation of flow, i.e.

$$p_p(L, t) = p_{d_i}(0, t) \quad \text{and} \quad q_p(L, t) = \sum_i q_i(0, t), \quad (6)$$

where, the subscripts p and d_i ($i = 1, 2$) denote the parent and daughter vessels, respectively.

At the terminal vessels, a Windkessel model (represented by an $R_1 C_p R_2$ circuit) is used to prescribe the outflow boundary condition (see Fig. 2c) by computing input impedance $Z_{wk}(L, \omega)$ as

$$Z_{wk}(L, \omega) \equiv \frac{P(L, \omega)}{Q(L, \omega)} = R_1 + \frac{R_2}{1 + i\omega R_2 C_p}, \quad (7)$$

where $P(L, \omega)$ and $Q(L, \omega)$ are the pressure and flow in the frequency domain, $\omega = 2\pi/T$ is the angular frequency and T is the length of the cardiac cycle. R_1, R_2 (mmHg s/ml) denote the two resistances, and C_p (ml/mmHg) is the capacitance. Moreover, the total peripheral resistance is $R_T = R_1 + R_2$, where R_1 represents the resistance of the imaginary blood vessels immediately beyond the terminal vessel (proximal vasculature) and R_2 is the resistance of the distal vasculature, whereas C_p denotes the total peripheral compliance of the vascular region in question. Similar to Qureshi et al. (2017), $Z_{wk}(L, \omega)$ relates the pressure and flow at the outlet of each terminal vessel via a convolution integral over T .

2.5 Parameter values

The model parameters are divided into three groups: hemodynamics $\Phi_h = \{T, \nu, \rho, \delta\}$, vessel wall stiffness $\Phi_{w.lin} = \{\beta\}$ for the linear wall model and $\Phi_{w.nlin} = \{p_1, \gamma\}$ for the non-linear wall model, Windkessel $\Phi_{wk} = \{R_1, R_2, C_p\}$ for the vascular beds.

Hemodynamic parameters are assumed constant. For each mouse (control and hypertensive), the length of the cardiac cycle $T = 1/\text{HR}$ (s) is extracted from the data. (Mean HR values for each group are given in Table 1.) The blood density $\rho = 1.057$ g/ml (Riches et al. 1973) and the kinematic viscosity $\nu = 0.0462$ cm²/s, measured at a shear rate of 94 s⁻¹ (Windberger et al. 2003). These values represent average values for mice. As discussed earlier, the boundary layer thickness is δ approximated by $\sqrt{\nu T/2\pi} \approx 0.03$ cm for the representative mice, which is kept constant throughout the network. This approximation gives a relatively flat velocity profile in the larger vessels and an almost parabolic profile in the smaller vessels.

The nominal vessel wall parameters for the linear and nonlinear wall models are approximated by combining an analytical approach, involving linearization of the fluid dynamics model, with available pressure and flow data. Since hemodynamic data are only available at one location (the main pulmonary artery), we let the vessel stiffness β be constant throughout the network. This assumption is supported by results by Krenz and Dawson (2003), who collated measurements of pulmonary vascular distensibility ($= \beta^{-1}$) from 26 studies in 6 different species reporting that within data variation the vessel distensibility is independent of the vessel diameter. A similar result was reported in our previous study (Lee et al. 2016), that compared 1D network models with homogenous (constant) and heterogeneous (vessel specific) wall distensibility. Results showed that heterogeneity does not affect pressure predictions in the MPA, though downstream predictions vary between the two cases. Yet without downstream data it is not possible to determine what strategy

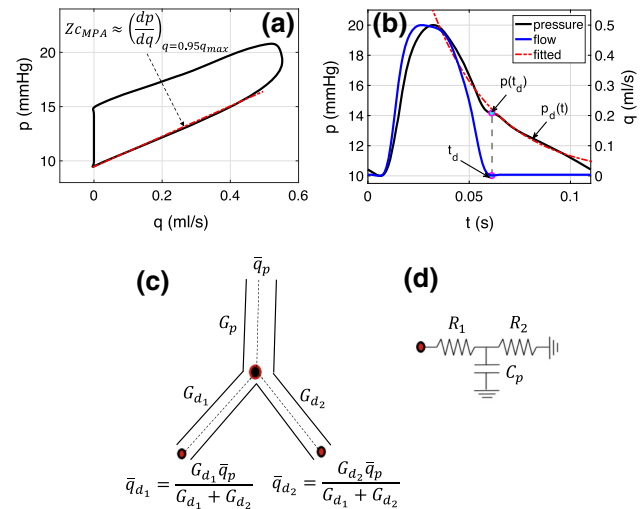


Fig. 3 Illustration of nominal parameter estimation for the linear elastic wall model and the Windkessel outflow conditions. **a** Approximation of Z_c from the slope of the pressure-flow loop during early ejection, **b** estimation of time constant τ by curve fitting, **c** flow distribution across a bifurcation to compute the resistance at the terminal points, **d** Windkessel model attached at the outlet of terminal vessels

gives the best physiological predictions, as a result we kept β constant along the network.

Linearization of Eqs. (2) and (3) about the reference state $(A, p) = (A_0, 0)$ provides an expression for the characteristic impedance Z_c (Nichols et al. 2011) as

$$Z_c = \frac{\rho c_0}{A_0} \Rightarrow c_0 = \frac{A_0 Z_c}{\rho}, \quad (8)$$

where c_0 is the wave speed at $p = 0$ (see “Appendix B” for the definition of c_0 for the linear ($c_{0.lin}$) and the nonlinear ($c_{0.nlin}$) wall models). For each mouse, Z_c is estimated from the slope of the pressure-flow loop during early ejection, using the “up-slope method” (see Fig. 3a) (Dujardin and Stone 1981) including 95% of the flow during ejection phase.

For the *linear wall model*, substituting c_0 in Eq. (8) with $c_{0.lin}$ gives

$$\sqrt{\frac{\beta}{2\rho}} = \frac{A_0 Z_c}{\rho} \Rightarrow \beta = \frac{2(A_0 Z_c)^2}{\rho}. \quad (9)$$

Similarly, for the *nonlinear wall model*, substituting c_0 in Eq. (8) with $c_{0.nlin}$ and using Eq. (9), gives

$$\frac{p_1}{\gamma} = \frac{(A_0 Z_c)^2}{\pi \rho} \Leftrightarrow \frac{p_1}{\gamma} = \frac{\beta}{2\pi}, \quad (10)$$

where β is given by Eq. (9) and p_1/γ is the “stiffness” of the nonlinear wall model. To fully specify the nominal (initial) values for the parameter inference (see Sect. 2.6 and Table 4), we set $\gamma = 2$ and $p_1 = \beta/\pi$. These values give $A_\infty = 2A_0$

cm^2 . Note that Eq. (10) is only valid if both the linear and nonlinear models incorporate the same value of A_0 at $p = 0$.

Nominal parameters for outflow boundary conditions must be computed for each terminal vessel. A priori values for these parameters can be obtained from distributing the total peripheral resistance computed in the MPA ($R_T = \frac{\bar{p}-p_c}{\bar{q}}$, the ratio of the mean pressure gradient $\bar{p} - p_c$ to mean flow) to each terminal vessel j as

$$R_{T,j} = \frac{\bar{p}}{\bar{q}_j},$$

where \bar{q}_j is the mean flow in vessel j . This expression is valid, under the assumption that capillary pressure p_c drops to zero and that mean pressure \bar{p} remains constant across the arterial network. The flow to vessel j is estimated by applying Poiseuille's law recursively at each junction, giving

$$\bar{q}_{d_i} = \frac{G_{d_i}}{\sum_i G_{d_i}} \bar{q}_p, \text{ where } G_{d_i} = \left(\frac{\pi r_0^4}{8\mu L} \right)_{d_i} \text{ for } i = 1, 2 \quad (11)$$

is the vessel conductance. Here q_{d_i} denotes the mean flow to vessel i . Similar to previous studies, e.g. Raymond et al. (2009), the total resistance is distributed as $R_{1,j} = aR_{T,j}$ and $R_{2,j} = R_{T,j} - R_{1,j}$, where the a priori value of $a = 0.2$ (McDonald and Attinger 1965).

It is worth mentioning that alternative approaches involving Murray's law or combination of Murray's and Poiseuille's law [e.g. see Chnafa et al. (2018)] can be used to approximate the steady flow distribution within the network, which may yield different hemodynamic predictions without further tuning of the nominal estimates. Moreover, many studies [e.g. Alastruey et al. (2016)] set R_1 equal to characteristic impedance of the associated terminal vessel to impose a reflection free boundary condition. However, it is known that arteries experience wave reflection from the vascular bed. To account for this effect, many studies set R_1 independent of characteristic impedance as some fraction of the total resistance and [e.g. see Acosta et al. (2017)], the approach followed in this study as well.

Finally, as suggested by Stergiopoulos et al. (1995), the total vascular compliance C_T (defined in "Appendix A") can be calculated by estimating the time constant $\tau = R_T C_T$ by fitting data to an exponential function of the form

$$p_d(t) = p_d(t_d) \exp(-(t - t_d)/\tau), \quad (12)$$

where the diastolic pressure $p_d(t)$ decays in time (see Fig. 3b). Assuming that τ is constant throughout the network, the compliance $C_{p,j}$ for each Windkessel can be computed as

$$C_{p,j} = \frac{\tau}{R_{T,j}}. \quad (13)$$

2.6 Numerical simulations

Similar to previous studies (Olufsen et al. 2000, 2012), we use the two-step Lax–Wendroff method to solve the model equations in Sects. 2.2 and 2.3, for the arterial networks presented in Table 2. We combine data from Sect. 2.1 with methods described in Sect. 2.5 to estimate nominal parameters, specifying arterial wall stiffness and boundary conditions (Sect. 2.4). Convergence to steady state is ensured by running simulations until the least square error between consecutive cycles of pressure is less than 10^{-8} , taking about 6 cycles on average. For this study, we fixed the number of cycles to 7 for all mice.

To match the model to data, parameters inferred using optimization include $\Phi_{\text{lin}} = \{\beta, R_{T,j}, a, \tau\}$ for the linear model and $\Phi_{\text{nl}} = \{p_1, \gamma, R_{T,j}, a, \tau\}$ for the nonlinear model. We define the objective function using sum of squared errors (mmHg^2) as

$$S(\Phi) = \sum_{n=1}^N (p_n - p(t_n; \Phi))^2, \quad (14)$$

where N is the length of the time vector spanning one cardiac cycle, p_n is the measured pressure, $p(t_n; \Phi)$ is the computed pressure from the inlet of the MPA, and Φ are the parameters to be optimized using the linear or the nonlinear wall models. We use the function *fmincon* in MATLAB under the sequential quadratic programming (SQP) gradient-based method (Boggs and Tolle 2000) to solve the associated least squares estimation problem

$$\tilde{\Phi} = \arg \min S(\Phi).$$

For the representative control mouse, optimization executed in parallel on an iMac (3.1 GHz Intel Core i5, 16 GB RAM, OS 10.12.6) initializing the parameters with 20 values drawn from a Sobol sequence with elements within the specified domain, consisting of an open interval around the nominal estimates. Results showed no signs of multimodality, and the optimization algorithm converged to a unique minimum regardless of starting point (see Figs. 11–13 in "Appendix E"). On average convergence required 28 and 52 iterations for the linear and the nonlinear models, respectively. To reduce computational efforts, efficiency and faster convergence, we conducted the optimization procedure for the remaining mice by initializing the parameters with four initial values, including the nominal and nearby values. Nominal values for individual mice are given in Table 4 ("Appendix C"), whereas upper and lower bounds as well as averaged optimal parameters are given in Tables 5 and 6 in "Appendix D." The algorithm was iterated until the convergence criterion was satisfied with a tolerance $< 10^{-8}$ mmHg.

2.7 Model analysis

Similar to Qureshi and Hill (2015) and Qureshi et al. (2017), we analyze wave intensity and impedance spectra for further insight. Wave intensity analysis allows us to quantify the type and nature of the reflected waves in the time domain, whereas the impedance analysis provides a frequency domain signature, which as shown in Fig. 1 differs between the two groups.

Wave intensity analysis allows us to separate the simulated waveforms into their incident (+) and reflected (−) components assuming negligible frictional losses. By setting $q = Au$, where u is the fluid velocity, the incident and reflected waves can be approximated by

$$\Gamma_{\pm}(t) = \Gamma(t_0) + \int_0^T d\Gamma_{\pm}; \quad \Gamma = p \text{ or } u.$$

$$\text{Here } dp_{\pm} = \frac{1}{2}(dp \pm \rho c du), \quad du_{\pm} = \frac{1}{2}\left(du \pm \frac{dp}{\rho c}\right), \quad (15)$$

and c is the PWV computed by Eq. (31) (“Appendix B”). Moreover, the composite waveforms $\Gamma = p$ or u are obtained by

$$\Gamma(t) = \Gamma_+(t) + \Gamma_-(t) - \Gamma(t_0), \quad t_0 = 0. \quad (16)$$

Time-normalized wave intensity WI_{\pm} ($\text{W}/\text{cm}^2/\text{s}^2$) is defined as

$$WI_{\pm} = (dp_{\pm}/dt) (du_{\pm}/dt). \quad (17)$$

WI_+ along with $dp_+ > 0$ or $dp_+ < 0$ characterize the incident waves as compressive or decompressive, while WI_- and $dp_- > 0$ or $dp_- < 0$ characterize the reflected waves as compressive or decompressive, respectively. Finally, we compute a simple wave reflection coefficient I_R as the ratio of the amplitudes of the reflected Δp_- to the incident Δp_+ pressure waves (Mynard et al. 2008, Li et al. 2016)

$$I_R = \frac{\Delta p_-}{\Delta p_+}, \quad (18)$$

which lumps the effects of low and high frequencies originating at spatially dispersed points of impedance mismatch throughout the vascular system. Although not desired here, a general frequency-dependent reflection coefficient can be computed as defined in Westerhof et al. (1972).

Impedance analysis (IA). Under the assumptions of periodicity and linearity, the pulsatile pressure and flow waveforms can be approximated by a Fourier series of the form

$$\tilde{s}(t_n) = \bar{S} + \sum_{k=1}^K \text{Re}[S_k e^{i(\omega_k t_n + \varphi_k)}]; \quad n = 0, \dots, N, \quad (19)$$

where $\tilde{s}(t_n)$ is the Fourier series approximation of the original waveform $s(t_n)$, $t_n = n/\text{Fs}$ is the time vector for a given sampling rate Fs , $N = T \times \text{Fs}$ is the length of the signal $s(t_n)$, $\omega_k = 2k\pi/T$ ($k = 1, \dots, K$) are the angular frequencies, \bar{S} is the mean of $s(t_n)$, and S_k and φ_k (rad) are the moduli and phase spectra, associated with each harmonic k , and K is the smallest resolution of harmonics required for the impedance analysis. Both, S_k and φ_k , are defined in terms of a_k and b_k , the coefficients of basic trigonometric Fourier series, i.e.

$$S_k = \sqrt{a_k^2 + b_k^2}, \quad \varphi_k = \tan^{-1}(b_k/a_k).$$

Setting $s(t_n)$ as $p(t_n)$ and $q(t_n)$ in Eq. (19), the impedance spectrum $Z(\omega_k)$ can be computed as ratios of harmonics of pressure to flow by

$$\begin{aligned} Z(\omega_k) &= \frac{P(\omega_k)}{Q(\omega_k)} \equiv \frac{\text{Re}[P_k e^{i(\omega_k t_n + \alpha_k)}]}{\text{Re}[Q_k e^{i(\omega_k t_n + \beta_k)}]} \\ &= \frac{P_k}{Q_k} \text{Re}[e^{i(\alpha_k - \beta_k)}] \equiv Z_k \text{Re}[e^{i\theta_k}], \end{aligned} \quad (20)$$

where P_k and Q_k are the moduli and α_k and β_k the phase angles of the pressure and flow harmonics, respectively. Z_k are the impedance moduli and $\theta_k = \alpha_k - \beta_k$ are the corresponding phases at a given frequency. Note if $\theta_k < 0$, then the k th pressure harmonic lags the k th flow harmonic, and vice versa. The zeroth harmonic is the total pulmonary vascular resistance (PVR).

2.8 Statistical analysis

We implement statistical analysis methods to study parameter interference and devise a model selection criteria to determine the ability of the linear and nonlinear wall models to predict hemodynamics.

Parameter inference. Optimized parameters and hemodynamic quantities are compared to assess changes with hypertension. For this analysis, we compare predictions of total vascular resistance (R_T), total vascular compliance (C_T), the compliance ratio (C_P/C_T), the resistance ratio (R_1/R_T), the wave reflection coefficient (I_R), and characteristic timescales (τ). Impact of the disease on a given quantity χ , averaged across the two groups, is inferred by computing an importance index η as a relative change in χ due to HPH as

$$\eta = \frac{\chi_{\text{HPH}} - \chi_{\text{CTL}}}{\chi_{\text{CTL}}}. \quad (21)$$

Model selection criterion. The 1D fluid dynamics model is coupled with a linear and a nonlinear wall model, leading to

four-dimensional (4D) and five-dimensional (5D) parameter spaces, respectively. To identify the model that is more consistent with the data, we employ a statistical criterion that trades off goodness of fit versus model complexity (i.e. the number of estimated parameters). To this end, we use the corrected Akaike Information Criterion (AICc) (Burnham and Anderson 2002) and the Bayesian Information Criterion (BIC) (Schwarz 1978) defined in Eqs. (22) and (23). The model with the lower AICc and BIC score is preferred.

$$\text{AICc} = -2 \log(\mathcal{L}) + 2D + \frac{2D(D+1)}{N-D-1}, \quad (22)$$

$$\text{BIC} = -2 \log(\mathcal{L}) + D \log N. \quad (23)$$

Here $\log(\mathcal{L})$ is the maximum log likelihood, D is the number of parameters in the model and N is the total number of measurements. If the noise is white, i.e. independent and identically Gaussian distributed, then $\log(\mathcal{L})$ is just a rescaled version of the sum-of-squares function $S(\Phi)$, defined in Eq. (14). However, a plot of the residuals (see Fig. 10 in Results section) indicates that the independence assumption is violated and that the correlation structure of the noise needs to be taken into account. Under the assumption of multivariate normal noise, the log likelihood is given by

$$\log(\mathcal{L}) = -\frac{1}{2} \log(\det(2\pi \Sigma)) - \frac{1}{2} \mathbf{r}^T \Sigma^{-1} \mathbf{r}, \quad (24)$$

where Σ is the covariance matrix and \mathbf{r} is the vector of residuals. For the estimation of Σ , we tried different approaches. We fitted an autoregressive moving average model, ARMA(p,q), to the time series of residuals, and identified the optimal parameters p and q by minimizing the BIC score. We then used the standard procedure proposed by Box and Jenkins (1970) to estimate the covariance matrix. Alternatively, we fitted a Gaussian process (GP) to the time series, using a variety of standard kernels: squared exponential, Matérn 5/2, Matérn 3/2, neural network kernel and a periodic kernel; see Rasmussen and Williams (2006) for details.

For the BIC and AICc scores, we need the maximum likelihood configuration of the parameters. This would require an iterative optimization scheme, where for each parameter adaptation, the covariance matrix would have to be recomputed. As this would lead to a substantial increase in the computational costs, we approximated the maximum likelihood parameters by the parameters that minimize the residual sum-of-squares error of Eq. (14).

3 Results

In this section, we present results of numerical simulations predicting pressure and flow waveforms along the pulmonary

arterial network for a representative control and hypertensive mouse followed by a comparison of estimated parameter values.

3.1 Hemodynamics

Figure 4 shows optimized pressure and flow waveforms for a representative control (left) and hypertensive (right) animal using the linear (dashed) and nonlinear (solid) wall models. Results were obtained estimating the least squares error between measured and computed waveforms in the MPA. The box and whisker plot (Fig. 4a) summarizes the least squares errors S (reported in Table 6 in “Appendix D”) comparing the measured and computed waveforms in the MPA (vessel 1). Results show that both wall models (linear and nonlinear) are able to fit the data well, and the least squares error is smaller for the hypertensive animals.

Even though both models provide similar fits in the MPA, the two wall models lead to different predictions in the downstream vasculature. For the control mouse, the nonlinear wall model leads to higher pressure in the downstream vasculature for the control mouse. With the linear wall model, the mean pressure drops ($\Delta \bar{p}_{\text{lin}} \approx 4$) mmHg from the MPA to the terminal vessels, whereas for the nonlinear model $\Delta \bar{p}_{\text{nl}} \approx 2$ mmHg. Moreover, the nonlinear wall model predicts a notch in the pressure and flow waveforms during the ejection phase, not observed with the linear wall model (displayed in panels 2, 8 and 13). Without more data from the downstream vessels, we are not able to validate which model is more accurate. Finally, it should be noted that these differences cannot be observed in predictions with the hypertensive animal, likely since the vessel wall is significantly less compliant.

Figure 5, depicting the pressure-area relationship in the MPA, gives further insight into the behavior of the linear and nonlinear wall mechanics. As expected, results show that for both groups the nonlinear wall model yields area predictions that are concave down implying increased stiffening at higher pressures. Higher compliance in control animals leads to more significant deformation despite the observation that the unstressed radius is larger in the hypoxic animals ($r_0 = 0.051 \pm 0.005$ vs. 0.047 ± 0.002 cm, from Table 2). Another interesting observation is the larger MPA area, for the control animal, predicted by the nonlinear wall model at a given working pressure. This could be a consequence of not being able to constrain the vessel area during the optimization, of correlations among the estimated parameters (e.g. if the vessel stiffness β (linear model) or p_1/γ (nonlinear model) are correlated with the proximal resistance r_1 , the two models may place optimal estimates at different stiffness/resistance ratios), or lack of data in the downstream vasculature.

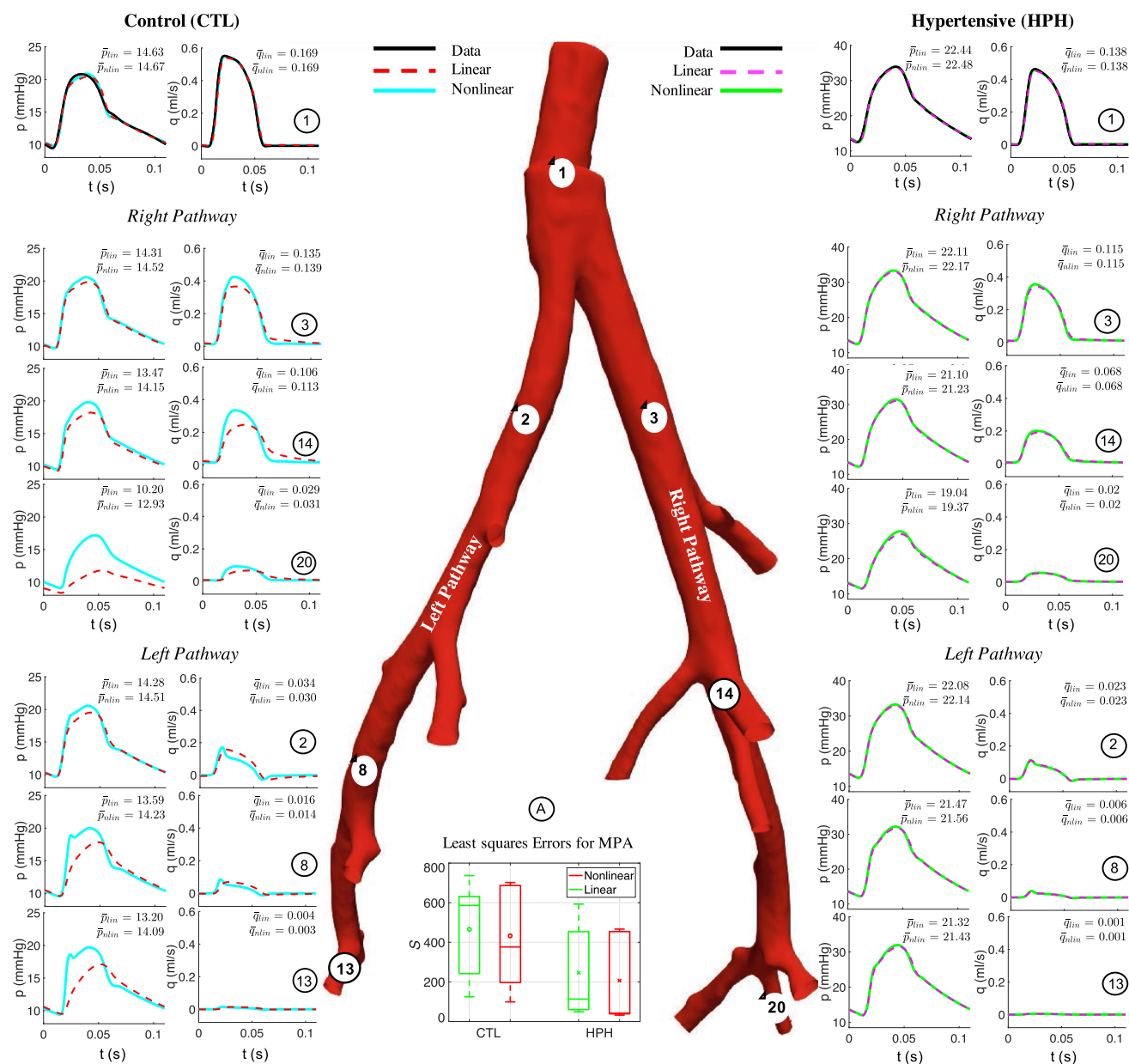


Fig. 4 Pressure and flow predictions along the pulmonary arterial network using linear (dashed line “- -”) and nonlinear (solid lines “—”) wall models. Results are shown for a representative control (left) and

hypertensive (right) mouse. The center panel **A** shows the least squares error averaged across CTL and HPH groups

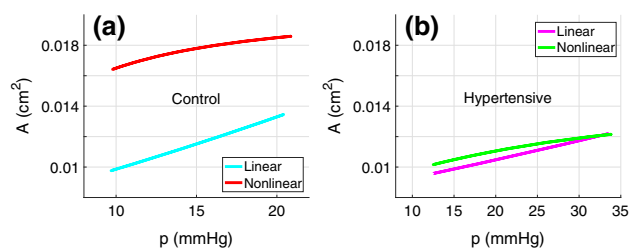


Fig. 5 Pressure-area plots corresponding to the linear and nonlinear wall models at the midpoint of the MPA for the control mouse (a) and hypertensive mouse (b)

3.2 Parameter estimates

Figure 6 summarizes the variation in optimized parameters for the two groups. Parameters, used to generate Fig. 6, along with *P* values assessing the significance of change due to HPH, are given in Table 6 in Appendix D.

The arterial wall stiffness is larger in mice with HPH (a–c). This claim is supported by a statistically significant increase in the stiffness parameters for both models. For the linear model, a significantly larger value of the stiffness parameter

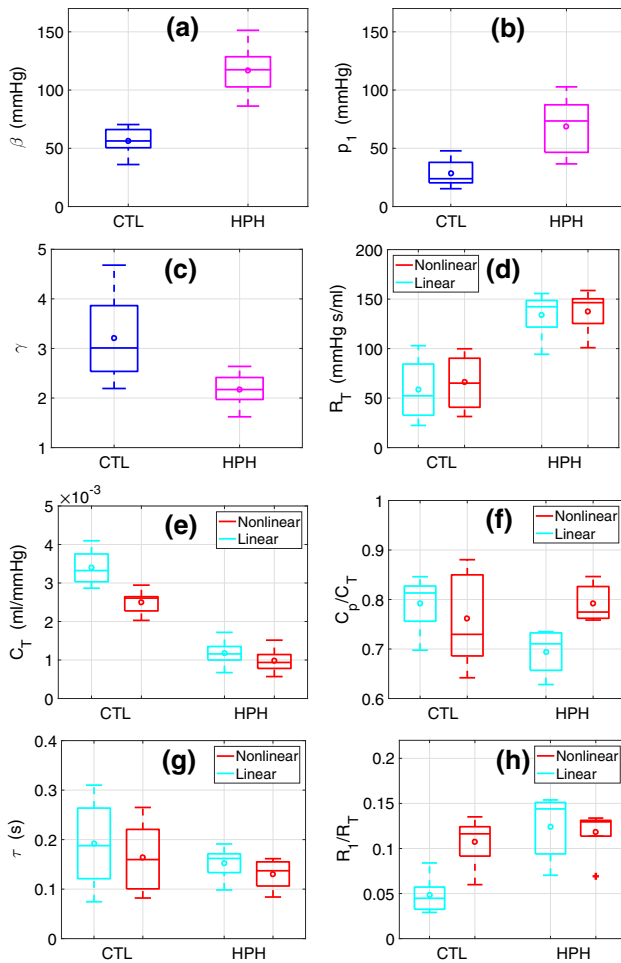


Fig. 6 Box and whisker plots summarizing the optimized parameter values for the CTL ($n = 7$) and HPH ($n = 5$) groups. On each box, the horizontal bar represents the population median, whereas the circle represents the population mean, the edges of the box are the 25th and 75th percentiles, the whiskers extend to the most extreme data points the algorithm, with the exception of outliers, which are plotted with a red plus sign. Top: **a** stiffness (β), **b** half width pressure (p_1), **c** maximal area (γ), **d** pulmonary vascular resistance (R_T). Bottom: **e** total vascular compliance (C_T), **f** peripheral-to-total compliance ratio (C_p/C_T), **g** characteristic timescale τ , and **h** resistance ratio $a = R_1/R_T$. Parameter values for individual mice using both models as well as a P values assessing the significance of change due to HPH are provided in Table 6 in “Appendix D”

β is estimated (a) ($P < 0.01$). For the nonlinear wall model, increased stiffness is predicted by an increase in the parameter p_1 ($P < 0.01$) representing the half width pressure (b), and a decrease in the constant γ ($P < 0.05$), representing the maximally expanded area (c). This is not surprising since β and p_1 have the same units and are proportional (see Eq. (10)). In addition, smaller γ leads to a smaller maximal area A_∞ [see Eq. (5)], indicating stiffer walls.

Compliance distributions between the network (C_v) and the vascular beds (C_p) are shown in Fig. 6e, f. Here the total compliance (C_T) for the entire vasculature is computed as

$$C_T \equiv C_v + C_p = \sum_i C_{v,i} + \sum_j \hat{C}_{p,j}, \quad (25)$$

where C_v is the total network compliance obtained as a sum of compliance estimates $C_{v,i}$ for each vessel i , computed for the linear or nonlinear wall models as functions of the diastolic blood pressure and area [Eqs. (28) and (29) in “Appendix A”], while $\hat{C}_{p,j} = (R_{2,j}/R_{T,j})C_{p,j}$ is the weighted compliance, computed as suggested by Alastruey et al. (2016), where $C_{p,j}$ denote the Windkessel capacitance [Eq. (7)] associated with each terminal vessel j .

Results show that the total vascular compliance C_T decreases with hypertension ($P < 0.01$) (Fig. 6e). Comparing with Fig. 6a–d, this behavior is anticipated given the reciprocal relations between vessel compliance and stiffness [Eqs. (28) and (29)] and peripheral compliance and total resistance (Eq. 13). The nonlinear model predicts a smaller compliance for both groups due to an increased stiffening with pressures ($P < 0.01$). Figure 6f shows the compliance distribution via the ratio C_p/C_T . Results with the linear wall model reveal that C_p reduces to 70% of C_T ($P < 0.01$) under hypertensive conditions (compared to 80% under control), indicating that vascular beds have been remodeled more by the disease. On the contrary, we found that nonlinear wall model predicts an increase in the ratio C_p/C_T of 80% in hypertension compared to 76% under control conditions. However, we found this change to be statistically insignificant ($P > 0.05$).

The total vascular resistance R_T is computed as

$$\frac{1}{R_T} = \sum_j \frac{1}{R_{T,j}} \quad \text{where} \quad R_{T,j} = R_{1,j} + R_{2,j}, \quad (26)$$

where j is the terminal vessel index. Its distribution within the vascular beds is depicted in Fig. 6d, h. In this study, we estimated the proximal and distal components $R_{1,j}$ and $R_{2,j}$ as described in Sect. 2.6. Results show that for both wall models R_T increases under hypertensive conditions (d) ($P < 0.01$). For the linear wall model, this increase is dominated by a significant increase in R_1 , evidenced by the increase in the resistance ratio R_1/R_T (h) ($P < 0.01$). Although R_1/R_T also slightly increases for the nonlinear model, the increase is statistically insignificant ($P > 0.05$).

The characteristic timescale $\tau = R_T C_T$ decreases under hypertensive conditions (Fig. 6g). Although, the nonlinear model predicts a smaller τ for all animals, the change in τ is statistically insignificant ($P > 0.05$) for both the linear and nonlinear wall models.

3.3 Wave intensity analysis

Results of the wave intensity analysis (WIA) allow us to investigate the behavior of the incident and reflected waves.

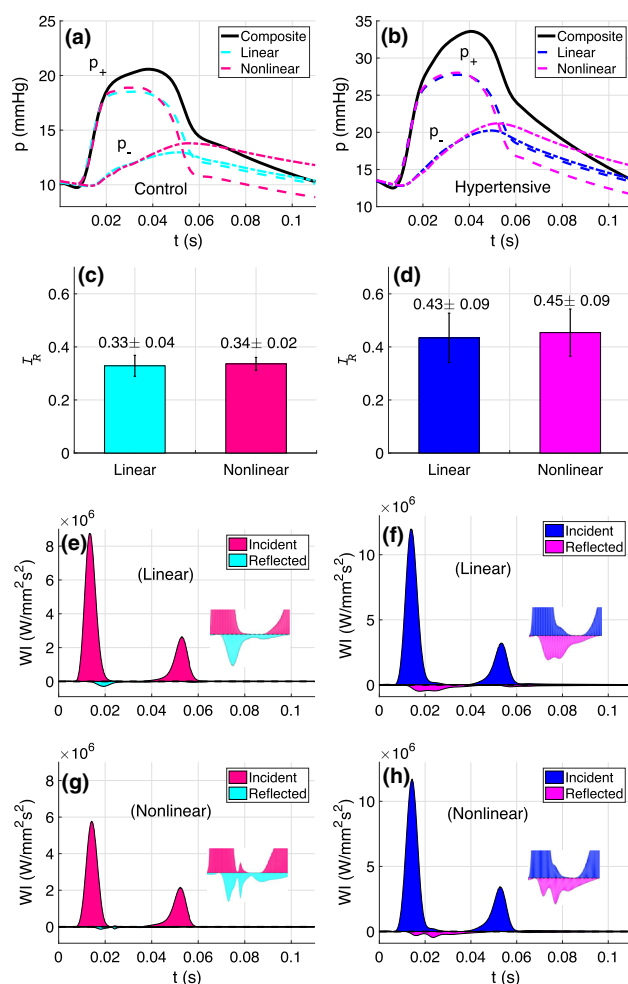


Fig. 7 Wave intensity analysis comparing the linear and nonlinear wall models for the control (a, c, e, g) and the hypertensive (b, d, f, h) mice. a, b Separation of the pressure wave into its incident and reflected components. The solid black curves represent the composite pressure waveforms, c, d the reflection coefficients averaged across the CTL and HPH groups. e–h The associated wave intensity profiles

Separation of the pressure and flow velocity waves into their incident and reflected components requires estimates of PWV (see Eq. (15)), which for the data at best can be approximated as constant. Moreover, since the resulting patterns of the reflected waves are sensitive to the PWV estimation technique (Qureshi and Hill 2015), in this study, the wave intensity analysis is only performed on the simulated waveforms for which the dynamic PWV can be computed explicitly.

Figure 7 shows separation of the pressure waveforms (a, b) into their incident and reflected components and the associated wave intensities (e–h). The group averaged reflection coefficients I_R , quantifying the magnitude of the reflections, are shown in panels (c) and (d). Results show that the amplitudes of the reflected waves are bigger in the hypertensive mice (b) leading to a bigger wave reflection coefficient,

shown in panel (d). Similar to stiffness and resistance parameters, the increase in I_R was found to be statistically significant ($P < 0.05$ and $P < 0.01$ for the linear and nonlinear wall models, respectively). Moreover, the effects of elastic nonlinearities on the amplitudes of the incident and reflected waves are minor (the increase in I_R is negligible across the two models) (c, d).

Figure 7e–h presents the wave intensity profiles associated with the separated pressure and velocity waves. The inner panels show zoomed intensities around peak systole. Again, the amplitude of the incident wave is higher for hypertensive mice [compare panels (e, g) with (f, h)]. For both groups, the nonlinear wall model gives rise to a smaller amplitude incident wave (compare panels e–h). Similar patterns are observed for the reflected waves. One notable difference, for both groups, is that the nonlinear model gives rise to more oscillations of the reflected wave.

3.4 Impedance analysis

Figure 8 depicts the impedance moduli $|Z|$ and phase spectra θ computed from the measured and simulated waveforms. Dashed lines show simulation results and solid black lines show data. Panels (a, c, e, g) show results from a control mouse and panels (b, d, f, h) show results from a hypertensive mouse. The impedance spectra were generated using Eq. (20) and plotted for the first 14 harmonics including the mean component (zeroth harmonic).

While time-varying simulations fit the data well, Fig. 8 shows characteristic differences in frequency domain signatures between the linear and nonlinear wall models. First, the zeroth frequency components do not vary between models. Comparison of moduli spectra (a–d) show that the linear wall model better captures the frequency response of the original system. However, both models miss the spike in the impedance moduli at the third harmonic (about 30 Hz) observed for the representative control mouse (a, c). This should be contrasted with results from the hypertensive animal, where both models predict the low-frequency behavior well (b, f). At higher frequencies, particularly after the ninth harmonic, the nonlinear wall model deviates from the measured impedance. In addition, the associated phase (θ) dips below zero indicating persistence of pressure harmonics, which precede the flow harmonic. Again, the linear wall model deviates less at higher frequencies and its phase oscillates about zero.

3.5 Statistical analysis

In this section, we compare estimated hemodynamics quantities pertinent to analysis of disease progression in HPH mice. To do so, we calculate an importance index (η) computed

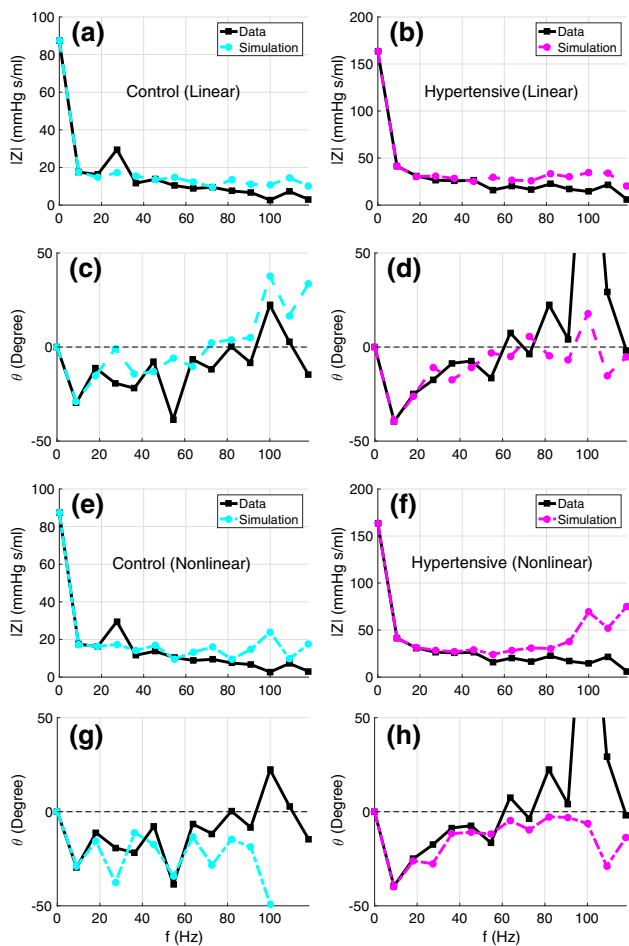


Fig. 8 Impedance spectra comparing the effects of linear (dashed line “—”) and nonlinear wall models (dashed dotted line “-.-”) compared to data (solid black lines) for a control (cyan) and a hypertensive (magenta) animal. Impedance moduli (importance of essential hemodynamic, **b**, **e**, **f**) and phase spectra (**c**, **d**, **g**, **h**) are plotted for the first 14 harmonics

from Eq. (21) using quantities averaged across the CTL and HPH groups.

Figure 9a shows predictions of η for the essential cardiovascular quantities (summarized in Table 1), whereas Fig. 9b does the same for the model parameters. Positive or negative values indicate an increase or a decrease in the quantity due to HPH. Moreover, a value of 1 (or -1) denote a 100% change in the quantity.

Results show that peripheral vascular resistance (R_T) and compliance (C_T , C_V , C_P) significantly contribute to differentiating between control and disease for the hypertensive animals ($\eta > 1$), whereas the resistance ratio R_1/R_T is important for predictions with the linear model ($\eta = 1.5$), but not for predictions with the nonlinear model $\eta = 0.1$. A similar observation was made for the nonlinear stiffness parameters, p_1/γ that is more important than the linear stiffness parameter β . Though both of these contributed significantly to distinguishing control versus hypertension.

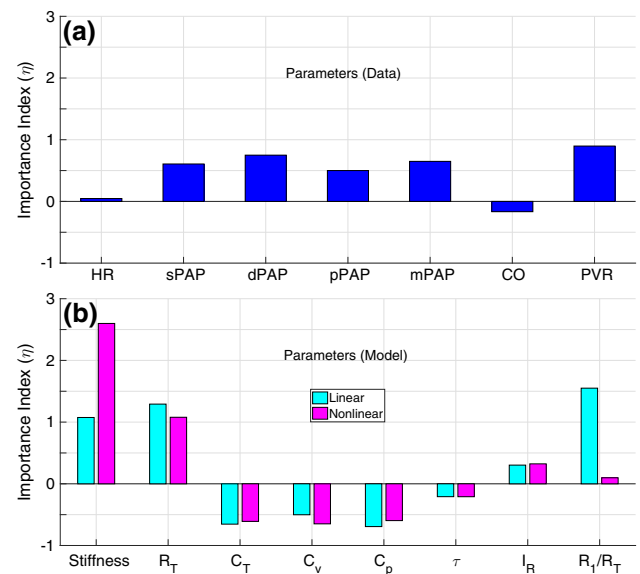


Fig. 9 **a** Importance of essential hemodynamic parameters computed comparing model predictions with data. See Table 1 for abbreviations on the abscissa. The figure show predictions of arterial stiffness β for the linear and p_1/γ for the nonlinear model. In addition, we compare predictions of total vascular resistance (R_T), total vascular compliance (C_T), total network (vessel) compliance (C_V), total peripheral (vascular bed) compliance (C_P), characteristic time constant (τ), wave reflection coefficient (I_R), and resistance ratio (R_1/R_T)

Finally, the wave reflection coefficient I_R and the time constant τ also differ between control and disease but at a smaller scale ($\eta < 0.5$).

Finally, we use statistical model selection criteria to determine which wall model is more consistent with the available hemodynamic data. Since the simple least squares error shows no difference between the two wall models for the hypertensive mouse, the model selection was done for the representative control mouse only. Specifically, we employ two model selection criteria (AICc and BIC), and model the residual correlation using the statistical ARMA model, and the GP models with different kernels (squared exponential, Matérn 3/2, Matérn 5/2, neural network and periodic kernel), as described in Sect. 2.8. We estimated the hyperparameters of the GP covariance matrices from the time series of residuals plotted in Fig. 10 by maximum likelihood. This was done by either using standard optimization algorithms involving maximizing the combined likelihood for the linear and the nonlinear models (Rasmussen and Williams 2006), or by separately finding the hyperparameters for the linear and the nonlinear models and then averaging the covariance matrices. Since the correlation structure of the noise depends on the experimental protocol and is independent of the model assumptions, the latter approach can be implemented under the constraint that the covariance matrices are the same for both wall models. We found that both approaches yield similar results to optimizing the GP hyperparameters for the

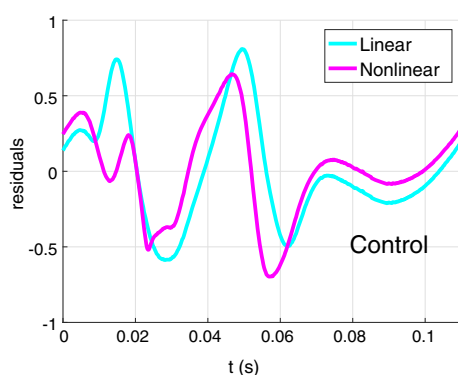


Fig. 10 Residual time series, as given by the difference between the measured and the simulated pressure signal corresponding to the linear and nonlinear wall model

residuals of both wall models. For simplicity, we applied the latter procedure to the ARMA model as well.

All the GP models and the ARMA model were consistent in indicating lower AICc and BIC scores for the linear model compared to the nonlinear model, see Table 3. This implies that the linear model is preferred according to AICc and BIC.

4 Discussion

In this section, we discuss our findings in physiological (CTL vs. HPH) and modeling (Linear vs. Nonlinear wall mechanics) contexts.

4.1 Inference of disease progression: CTL versus HPH

In this study, we used micro-CT images to set up anatomical networks and combined them with hemodynamic predictions from a 1D model. We calibrated the model for seven control and five hypertensive mice, estimating key parameters (large vessel stiffness, peripheral vascular resistance, peripheral vascular compliance, wave reflection coefficient) that characterize vascular remodeling due to pulmonary hypertension.

Stiffness, compliance, and resistance. Comparison between the two groups (independent of the wall model) shows that hypertensive mice exhibit stiffer vessels both prox-

imally (within the network), and in the microcirculation (represented by the Windkessel models) reflecting a rather advanced stage of HPH. In this study, we attribute changes in total resistance R_T and compliance C_T to both functional (vasoconstriction) and structural (rarefaction) microvascular remodeling, known to elevate the mPAP (Qureshi et al. 2014; Wang and Chesler 2011). Changes in the large vessel parameters, p_1 and γ for the nonlinear model and β for the linear model as well as the unstressed vessel radius r_0 , contribute to the stiffness of the proximal vessels.

The results presented here show that the parameter with the largest impact is R_T . This is expected physiologically, as the disease progresses from the microvasculature to the large vessels. Almost as significant are changes in vessel stiffness (p_1/γ and β) reflecting that the large vessels also stiffen, but with a relatively small change in r_0 indicating that the large vessels have not decreased in size. These results also reveal a significant decrease in total vascular compliance with hypertension (Fig. 6e). As for the compliance distribution, the average values of $C_p/C_T \approx 80\%$, in both groups, suggest that the majority of the compliance is located in the vascular beds (Fig. 6f). This is unlike the systemic circulation where the aorta is the main contributor to compliance, contributing more than 50% of the total systemic compliance (Ioannou et al. 2003). Our finding of $C_p/C_T > 0.7$ for the CTL animals compliments the experimental observation by Presson et al. (1998), who found $\sim 65\%$ of the total pulmonary compliance in vessels with diameters $< 40 \mu\text{m}$. The smallest vessels in our networks have diameters of $260 \mu\text{m}$ for the control mice (vessel #5 in Table 2) and $300 \mu\text{m}$ for the hypertensive mice (vessel # 13 in Table 2). Thus, the vessels in diameter range between these diameters and $40 \mu\text{m}$ were also lumped into the Windkessel models, justifying a value of $C_p > 65\%$. So, the reasons we may be getting a relatively small network compliance ($C_v \approx 20\%$) could be due to the fact that not enough of the large network is included in the model, and that adding more generations may change the current value of C_p/C_T .

Moreover, the linear wall model shows a significant decrease in the compliance ratio C_p/C_T under HPH, suggesting a greater compliance loss due to remodeling of the vascular beds than for the large vessels. Although, the non-

Table 3 AICc and BIC scores for the linear and nonlinear wall model with the covariance matrices obtained using ARMA model and five Gaussian process (GP) models with squared exponential, Matérn 3/2, Matérn 5/2, neural network and periodic covariance kernels

Score type & wall model	ARMA	GP squared exponential	GP Matérn 3/2	GP Matérn 5/2	GP neural network	GP periodic
AICc linear	−4418	−4260	−4304	−4396	−4436	−4252
AICc nonlinear	−4279	−4152	−4198	−4251	−4352	−4150
BIC linear	−4401	−4243	−4288	−4380	−4420	−4236
BIC nonlinear	−4254	−4131	−4177	−4230	−4330	−4129

Lower AICc and BIC values (in bold) indicate the better mathematical model

linear wall model shows the opposite by predicting a slight increase (3%) in C_p/C_T and indicating a greater remodeling of the larger vessels, these results were statistically insignificant. Our analysis of compliance distribution reflects the dominant role of vascular bed stiffening in the disease progression, suggesting C_p to be an important bio-marker of disease detection and progression.

In summary, these findings suggest that the hypertensive animals analyzed here exhibit remodeling of the entire vasculature, with distal vascular remodeling playing a dominant role in elevating arterial blood pressure.

Wave reflection. Analysis of computed waveforms show existence of backward compression waves during late systole and, contrary to the observation about the pulmonary system in dogs (Hollander et al. 2001) and humans (Qureshi and Hill 2015), we did not detect a reflective decompressive wave in mice. Moreover, the wave reflection coefficient I_R is significantly higher in hypertension (Figs. 7c, d, 9). This observation can be explained by hypothesized proximal and distal remodeling. As shown in Fig. 7a, c, e, g, the system has some degree of compressive wave reflections under control conditions. During hypertension, the stiffer proximal vasculature causes augmentation of the incident pressure wave (compare the p_+ waves in Fig. 7a, b). In addition, comparison of the reflection coefficients I_R (compare Fig. 7c, d) reveals that reflection is increased in the hypertensive animals caused by remodeling of the vascular beds. The net increase in I_R during hypertension exhibits the combined effect of proximal and distal vascular remodeling, i.e. dominated by the distal remodeling, on the main pulmonary arterial pressure.

The advantage in using I_R is that it provides insight into systemic effects rather than focusing on either small or large vessels, and as such I_R could be an important indicator of disease progression. However, its usefulness cannot be fully analyzed in the current model since it employs a fixed inflow, simulating the cardiac compensation scenario during which the cardiac output is maintained with hypertension (Acosta et al. 2017). A model including a heart component [e.g. Acosta et al. (2017); Formaggia et al. (2006); Mynard and Smolich (2015)] and 1D vascular beds [e.g. Chen et al. (2016); Olufsen et al. (2012); Qureshi et al. (2014)] would be ideal to analyze the complex role of wave reflections in disease progression. Moreover, it is worth mentioning that the reflection coefficient I_R is an aggregated measure of reflections under control and hypertensive conditions. Implicitly, it assumes that waves at the fundamental (i.e. the HR) and nearby nonnegative frequencies are the major contributors to the reflection (Segers et al. 2007), undermining the significance of high frequency waves, as shown in earlier studies by Westerhof et al. (1972) and Guan et al. (2016). Although, a frequency-dependent reflection coefficient could be computed using the impedance spectra in Fig. 8, we anticipate

difficulties, due to the calculation of characteristic impedance in the frequency domain (Qureshi et al. 2018). Nevertheless, changes in the reflection coefficient at various frequencies due to pulmonary hypertension merits a separate detailed investigation.

Impedance analysis. Overall, the characteristic features of the impedance spectra resemble those reported by Nichols et al. (2011) (Ch. 16). We note that the impedance moduli are higher in hypertension, whereas the phase shows that it starts out negative and then crosses zero at higher frequencies. These results supplement observations from Vanderpool et al. (2011), who studied the impedance spectra using in vitro pulsatile hemodynamics in isolated lungs of the same type of mice.

The results of low-frequency components are more subtle. One observation is that the low-frequency response is more dynamic in the control animals, reflecting that large vessels are more compliant. A characteristic feature that we were not able to reproduce for the representative control mouse was a pronounced third harmonic observed in control animals. To our knowledge, this feature has not been reported elsewhere, and could be a consequence of vessel tapering or wave propagation from the vascular beds (which are not included in this study), or it could be an artifact from cycle averaged data. Unfortunately we do not have access to the raw data to confirm or deny this characteristic.

In summary, pulmonary hypertension is characterized by a more resistive and less compliant vasculature with augmented wave reflections, associated with high blood pressure in the larger pulmonary arteries. This is in line with observations by Lankhaar et al. (2006) and Lungu et al. (2014) for patients with and without pulmonary hypertension. Lankhaar et al. (2006) used a 0D Windkessel model neglecting the effects of wave propagation and arterial stiffness, whereas Lungu et al. (2014) used a coupled 0D–1D model representing the pulmonary vasculature by a single vessel. In addition, we can confirm the experimental observations that the pulmonary compliance is uniformly distributed throughout the vasculature and just not confined to the largest vessels (Krenz and Dawson 2003; Presson et al. 1998). This makes pulmonary hypertension an intrinsically different disease than systemic hypertension. Overall, our analyses suggest that the disease state and progression is dominated by vascular bed remodeling playing a dominant role in altering the disease markers (resistance, compliance and reflections), whereas the large arterial remodeling is more of a consequence. It contributes to disease progression but at a later stage. Therefore, we suggest that not only should drug therapies focus on affecting the microvasculature (arterioles, capillaries and venules), but microvasculature should also be subjected to detail analysis, using noninvasive procedures like imaging, for a better understanding of disease progression.

4.2 Inference of disease progression: linear versus nonlinear wall mechanics

It is well known that arterial deformation acts nonlinearly imposing increased stiffening with increased pressure (Valdez-Jasso et al. 2011). Although, most studies confirming this behavior are done in systemic arteries (Eck et al. 2017; Langewouters et al. 1985; Valdez-Jasso et al. 2011), pulmonary arteries are composed of the same type of tissue and therefore should exhibit similar behavior under dynamic loading (Lee et al. 2016). To understand the effects of nonlinearities on hemodynamic predictions and parameter estimation, we implemented a linear mechanistic and a nonlinear empirical wall model. A qualitatively reasonable outcome, i.e. increased stiffening with pressure, in the form of nonlinear pressure–area curve is evident from Fig. 5. In the absence of actual data for the area deformation, the area predictions using the linear and nonlinear models cannot be validated. As discussed in the results section, the apparent difference in area predicted with the linear and nonlinear wall models for the control animal can be a result of several aforementioned factors which should be investigated further in future studies.

The nonlinear wall model. Previous empirical nonlinear stress strain models are formulated using sigmoidal functions, relating pressure and area, saturating at both high and low pressures (Langewouters et al. 1985; Valdez-Jasso et al. 2011). This type of model is characterized by an inflection point determined by a parameter representing the half-saturation (or maximum compliance) pressure. Valdez-Jasso et al. (2011) validated these models against dynamic loading data, from ovine thoracic descending aorta (TDA) and carotid artery (CA) under in vivo and ex vivo conditions, showing that pressure–area dynamics lie on the upper (concave down) part of the sigmoidal curves. While these models were able to fit data well, their estimates of the half-saturation parameter p_0 lie outside the known physiological range.

The advantage of the model used here is that it provides similar estimates, but uses one less parameter, eliminating the need to estimate p_0 a parameter that likely is unidentifiable. In this study, we set $p_0 = 0$. While the wall model still provides the typical sigmoid shape as the original Langewouters model, the point of inflection appears at zero pressure. Moreover, our model provides a basis for theoretical comparison with the linear model at a reference state $(A, p) = (A_0, 0)$, since under the small strain assumption, the nonlinear wall model in Eq. (4) approximates to

$$p \approx \frac{2\pi p_1}{\gamma} \left(\sqrt{\frac{A}{A_0}} - 1 \right) + O \left(\sqrt{\frac{A}{A_0}} - 1 \right)^2, \quad (27)$$

which is the linear model with $\beta = 2\pi p_1/\gamma$ [see Eq. (10)]. This property justifies the interchangeable use of $c_{0,\text{lin}}$ and $c_{0,\text{nl}}$ in Eq. (8), used to estimate nominal values for p_1 and γ .

In summary, simulations with the linear wall model are predominantly governed by the 0D boundary conditions, i.e. vascular beds, whereas the nonlinear model modulates both the 1D, i.e. large vessels, and 0D domain to predict hypertensive hemodynamics. This suggests that the linear wall model predicts greater remodeling of the vascular beds due to HPH. However, the general inferences about control and hypertensive hemodynamics, i.e. decreased total compliance, increased stiffness, resistance and amplitudes of wave reflections, remain the same.

The results shown here indicate that measurements in the MPA can be predicted with either wall model, but that predictions in the small vessels differ. Without more data confirming behavior in small vessels it is not possible to conclude which model is better. Moreover, we showed that in hypertensive animals both models provide comparable predictions, likely a result of increased vessel stiffness, but for the control animal elastic nonlinearities due to high compliance may have significant effects on the model predictions.

4.3 Model selection

To our knowledge, no previous 1D wave propagation studies have implemented statistical criterion for model selection. In this study, we have carried out statistical model selection to discriminate between the linear and the nonlinear wall model given available data in the main pulmonary artery using AICc and BIC scores. While we have made a parametric assumption about the measurement noise, we have taken its correlation structure into consideration by fitting a set of standard time-series models to the residuals. We have focused on the control mice, for which the difference between the linear and the nonlinear model was significant. Our results suggest that the linear model is preferred. One study by Valdez-Jasso (2010), examining wall properties used the Akaike Information Criterion (AIC) for selecting the wall model. Their results showed that for control animals (they studied sheep) the nonlinear wall model performs better, whereas for stiffer vessels, the linear model performs better. Their former conclusion is contradictory to our model selection analysis of control mouse but the later is consistent with our findings, which show no difference in the predictions using the linear and the nonlinear wall models. However, Valdez-Jasso (2010) only examined the stress–strain relation in single vessels in absence of fluid dynamics. It should be noted that results presented in this study were done using classical AICc and BIC selection criteria, which have an asymptotic justification. Better approximations that are less reliant on asymptotics are the

Watanabe–Akaike information criterion (WAIC) (Watanabe 2010) or the Watanabe–Bayesian information criterion (WBIC) (Watanabe 2013). However, these more accurate model selection methods, which we have explored in a recent proof-of-concept study (Paun et al. 2018), are based on Monte Carlo simulations and are thus computationally considerably more expensive.

4.4 Limitations

In this study, we did not account for the variation in network dimensions from mouse to mouse. This limitation stems from the experimental conditions, as we do not have hemodynamic and micro-CT lung image from the same animals. The network studied was set up to represent average vasculature from the two groups. We segmented vessels that could be found in all animals and used vessel length and diameters reflecting the average from each group. In future studies, we plan to examine the uncertainty associated with network variation in more detail. We also ignored the uncertainty in the hemodynamic data resulting from ensemble encoding of pressure and flow waveforms over multiple cardiac cycles. Although uncertainty quantification is beyond the scope of this study, it is an important aspect that may have significant impact on the parameter inference. Moreover, it is not clear from image studies if the individual vessels taper, thus the effects of vessel tapering were not considered in this study. Yet, it is known that tapering introduces significant augmentation of pressure along each vessel and throughout the network, which makes it a sensitive model parameter, which could be investigated. Other modeling limitations of this work include the use of a fixed inflow, a 0D vascular bed model terminated at capillary pressure of 0 mmHg. This assumption is unphysiological (Hellmes et al. 1949). However, its inclusion is expected to have an insignificant effect on the flow dynamics and parameter inference across healthy to diseased conditions. It would be more interesting to study this phenomenon within a more advanced framework for the outflow boundary condition [e.g. see Olufsen et al. (2012) and Qureshi et al. (2014)]. Moreover, in this study, we assumed a constant blood viscosity throughout the network. This is reasonable as the vessels included here are of the same order of magnitude. However, the Fåhræus–Lindqvist effect may become significant in studies examining larger networks including bigger variation in vessel diameters due to rapid progression to small caliber vessels. As for the comparison of linear and nonlinear wall models, the interaction of the wall parameters with the local hemodynamics should be investigated in more detail to understand the apparent difference in area prediction for the control animal. One aspect is the inclusion of minor frictional losses, which may have an effect for the control animal, but be insignificant under the higher operating pressure experienced by the hypertensive animal. Finally, the

model selection outcome is only valid for the current hemodynamic data, which is available from one location in the main pulmonary artery. The AICc and BIC scores may vary significantly if the waveforms are available from multiple locations within the network.

5 Conclusions

We found that the hypertensive mice display significant disease progression associated with remodeling within both large and small vessels. Microvascular remodeling characterized by reduced compliance, increased resistance, augmenting wave reflections and stiffened large vessels is associated with high blood pressure in the main pulmonary artery. We also conclude that both linear and nonlinear models can be used to predict the control and hypertensive hemodynamics in the MPA with high accuracy, yet the prediction in the smaller vessels and vascular beds differ. Without more data, it is not possible to select which model better reflects wave propagation along the entire network. These differences were only displayed for control mice, with more compliant vessels. For the hypertensive mice, both large and small vessels are almost rigid and the two models predict the same behavior. Although, the model selection criteria pick the linear wall model for the control mouse, these results should not be considered in the statistical context alone as the availability of more physiological data for optimization may alter the present outcome. Finally, analysis of network hemodynamics, wave intensities and impedance moduli indicates an increased presence of wave reflections using the nonlinear model. For this reason, parameter inference and characterization of normal and remodeled vasculature should be regarded as qualitative when using our nonlinear model.

Funding This study was supported by the National Science Foundation (NSF) awards NSF-DMS # 1615820, NSF-DMS # 1246991 and Engineering and Physical Sciences Research Council (EPSRC) of the UK, grant reference number EP/N014642/1.

Compliance with ethical standards

Conflict of interest The authors declare that they have no conflict of interest.

Appendix

A Vascular compliance

The volumetric compliance, defined as $C_v = dV/dp$ (ml/mmHg) for a cylindrical vessel with volume V , is computed from the linear (C_{lin}) and nonlinear (C_{nlin}) models. For a longitudinally tethered vessel i in the network

$$C_v = \frac{dV}{dp} \equiv L \frac{dA}{dp}, \quad (28)$$

where L is the fixed length of the vessel and dA/dp is computed from Eqs. (3) and (4), giving

$$C_{\text{lin}} = C_{0,\text{lin}} \left(\frac{p}{\beta} + 1 \right), \quad \text{and} \quad C_{\text{nl}} = C_{0,\text{nl}} \left(\frac{p_1^2}{p^2 + p_1^2} \right), \quad (29)$$

where C_0 denotes the reference compliance at $p = 0$, given by

$$C_{0,\text{lin}} = \frac{2A_0L}{\beta}, \quad \text{and} \quad C_{0,\text{nl}} = \frac{\gamma A_0L}{\pi p_1}. \quad (30)$$

B Pulse wave velocity

The pulse wave velocity (PWV), c (cm/s), is computed from the eigenvalues of the hyperbolic system of Eq. (2), from $\lambda_{1,2} = q/A \pm c$ where

$$c = \sqrt{\frac{A}{\rho} \frac{dp}{dA}} = \sqrt{\frac{AL}{\rho C_v}}. \quad (31)$$

Setting $C_v = C_{\text{lin}}$ and C_{nl} in Eq. (31) gives the squared PWV computed for the linear and nonlinear wall models, respectively

$$c_{\text{lin}}^2 = c_{0,\text{lin}}^2 + \frac{p}{2\rho},$$

$$c_{\text{nl}}^2 = c_{0,\text{nl}}^2 \left(\frac{\gamma}{\pi} \tan^{-1}(p/p_1) + 1 \right) \left(1 + (p/p_1)^2 \right), \quad (32)$$

where c_0^2 is the square of the reference PWV at $p = 0$, given by

$$c_{0,\text{lin}}^2 = \frac{\beta}{2\rho}, \quad \text{and} \quad c_{0,\text{nl}}^2 = \frac{\pi p_1}{\gamma \rho}. \quad (33)$$

We use PWV in wave intensity analysis, described in Sect. 2.7, for separating the incident and reflected waves.

C Nominal parameter values

As described in Sect. 2.5, nominal values for the nonlinear model are set as $p_1 = \beta/\pi$ and $\gamma = 2$ for all cases. Moreover, nominal values for $R_{T,j}$ are computed from R_T reported in the table above using methods described in Sect. 2.5 and the network dimensions stated in Table 2. For all cases, the resistance ratio $a \equiv R_1/R_T = 0.2$.

Table 4 Nominal values for wall parameters and compliance for individual mice in each group

Control	β_0 (mmHg)	R_{T_0} (mmHg s/ml)	τ_0 (s)
1	37.5	108	0.15
2	44.5	56	0.06
3	37.7	47	0.06
4	40.7	70	0.10
5	15.6	69	0.13
6	26.0	87	0.14
7	31.7	101	0.13
Hypertensive	β_0 (mmHg)	R_{T_j} (mmHg s/ml)	τ_0 (s)
1	150.6	164	0.09
2	56.8	107	0.11
3	123.8	163	0.15
4	100.7	154	0.13
5	78.5	143	0.11

D Optimized parameter values

For all cases, we optimized β , γ , and p_1 for the wall models, and the global scaling parameters r_1, r_2, c_1 for the Windkessel model, such that

$$R_{1,j} = r_1 R_{10,j}, \quad R_{2,j} = r_2 R_{20,j}, \quad C_{p,j} = c_1 C_{p0,j}$$

where 0 indicate the nominal quantity. Upper and lower bounds for the optimization intervals are given in Table 5.

Table 5 Bounds for optimization

Parameter	β	p_1	γ	(r_1, r_2, c_1)
Lower bound	β_0	$\beta_0/2\pi$	1	0.05
Upper bound	$2.5\beta_0$	$2\beta_0$	2π	2.5

E Convergence of optimization algorithm

To test the convergence of our optimization algorithm, we carried out repeated optimizations in four- and five-dimensional parameter spaces for the linear and nonlinear wall models, respectively. This was done only for the representative control mouse. Optimizations were initialized from 20 initial values, drawn using the Sobol sequence to uniformly cover the entire domain (i.e. predefined interval). Regardless of the starting value, the algorithm converged to the same values for a given parameter. Also, Fig. 13 shows the convergence to a unique minimum of the objective function

Control Linear

Parameters were computed back from optimized values of β , p_1 , γ , r_1 , r_2 and c_1 . Last row present the P value, computed using the *ttest* in the MATLAB, for all parameters inferred using the linear and nonlinear wall models. A P value < 0.05 indicates a significant change in parameter value due to HPH

β (mmHg), R_T (mmHg s/ml), C_T (ml/mmHg), I_R , $C_p/C_T(\%)$, a (dimensionless), p_1 (mmHg), γ (dimensionless), S : least square error

*Differences in these parameter values due to HPH is statistically insignificant

regardless of the starting point. For the sake of computational efficiency, parallel optimization was conducted starting from only four initial values for the remaining mice. Figures 11 and 12 show the optimization history (starting from 20 initial points) for the linear and nonlinear cases from the control mouse.

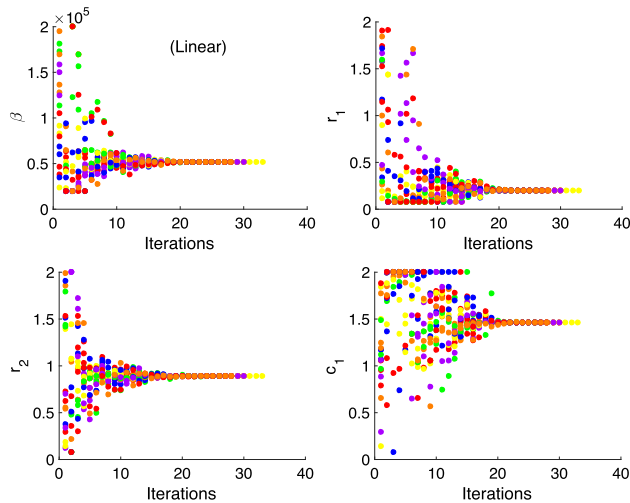


Fig. 11 Time history of optimization algorithm for the case of linear wall model. As a test case, 20 starting points were sampled from the parameter interval (vertical axis). Each color represents an iteration chain associated with a given starting point. All of them converged to the same final value. On average, it took 28 iterations to converge to an optimal value using the linear wall model

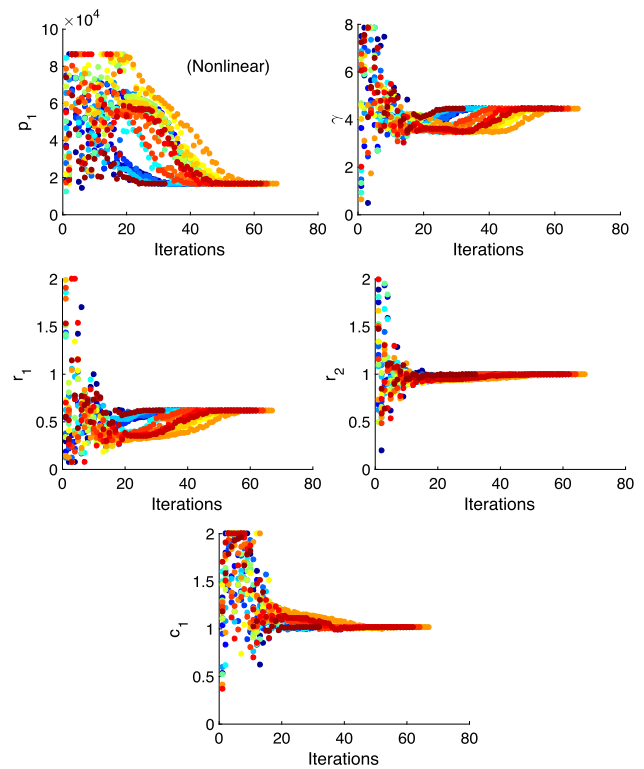


Fig. 12 Time history of optimization algorithm for the case of nonlinear wall model. As a test case, 20 starting points were sampled from the parameter interval (vertical axis). Each color represents an iteration chain associated with a given starting point. All of them converged to the same final value. On average, it took 52 iterations to converge to an optimal value using the nonlinear wall model

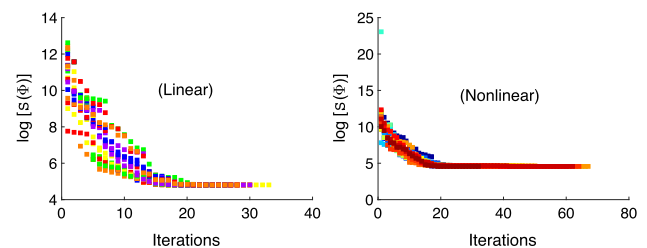


Fig. 13 Time history of objective function's values during the optimization process starting from 20 starting points. Each color represents an iteration chain associated with a given starting point. The plots are shown on a linear-log scale ($\log(S)$) both using the linear and the nonlinear wall models for the representative control mouse. Optimization converges to a minimum of objective function irrespective of the starting point

References

- Acosta S, Puelz C, Rivière B, Penny DJ, Brady KM, Rusin CR (2017) Cardiovascular mechanics in the early stages of pulmonary hypertension: a computational study. *Biomech Model Mechanobiol* 16:2093–2112
- Alastruey J, Xiao N, Fok H, Schaeffter T, Figueroa CA (2016) On the impact of modelling assumptions in multi-scale, subject-specific models of aortic haemodynamics. *J R Soc Interface*. <https://doi.org/10.1098/rsif.2016.0073>
- Arnold A, Battista C, Bia D, German YZ, Armentano RL, Tran HT, Olufsen MS (2017) Uncertainty quantification in a patient-specific one-dimensional arterial network model: EnKF-based inflow estimator. *ASME J Verif Valid Uncert* 2(1):14
- Antiga L, Piccinelli M, Botti L, Ene-Iordache B, Remuzzi A, Steinman DA (2008) An image-based modeling framework for patient-specific computational hemodynamics. *Med Biol Eng Comput* 46:1097–1112. <http://www.vmtk.org>
- Aslanidou L, Trachet B, Reymond P, Fraga-silva RA, Segers P, Stergiopulos N (2016) A 1D model of the arterial circulation in mice. *ALTEX* 33:13–28
- Blanco PJ, Watanabe SM, Dari EA, Passos MARF, Feijo RA (2014) Blood flow distribution in an anatomically detailed arterial network. *Biomech Model Mechanobiol* 13(6):1303–1330
- Boileau E, Nithiarasu P, Blanco PJ, Miller LO, Fossan FE, Hellevik LR, Donders WP, Huberts W, Willemet M, Alastruey J (2015) A benchmark study of numerical schemes for one-dimensional arterial blood flow modelling. *Int J Numer Method Biomed Eng*. <https://doi.org/10.1002/cnm.2732>
- Boggs P, Tolle J (2000) Sequential quadratic programming for large-scale nonlinear optimization. *J Comput Appl Math* 124:123–137
- Box GEP, Jenkins GM (1970) Time series analysis: forecasting and control. Holden-Day, San Francisco
- Burnham KP, Anderson DR (2002) Model selection and multimodel inference: a practical information-theoretic approach, 2nd edn. Springer, Berlin
- Castelain V, Hervé P, Lecarpentier Y, Duroux P, Simonneau G, Chemla D (2001) Pulmonary artery pulse pressure and wave reflection in chronic pulmonary thromboembolism and primary pulmonary hypertension. *J Am Coll Cardiol* 37(4):1085–1092
- Chen WW, Gao HG, Luo XY, Hill NA (2016) Study of cardiovascular function using a coupled left ventricle and systemic circulation model. *J Biomech* 49(12):2445–2454
- Chnafa C, Brina O, Pereira VM, Steinman DA (2018) Better than nothing: a rational approach for minimizing the impact of outflow strategy on cerebrovascular simulations. *AJNR Am J Neuroradiol* 39(2):337–343
- Dujardin JP, Stone DN (1981) Characteristic impedance of the proximal aorta determined in the time and frequency domain: a comparison. *Med Biol Eng Comput* 19:565–568
- Ellwein LM, Marks DS, Migrino RQ, Foley WD, Sherman S, LaDisa JF (2016) Image-based quantification of 3D morphology for bifurcations in the left coronary artery: application to stent design. *Catheter Cardiovasc Interv* 87:1244–1255
- Eck VG, Sturdy J, Hellevik LR (2017) Effects of arterial wall models and measurement uncertainties on cardiovascular model predictions. *J Biomech* 50:188–194
- Feldkamp LA, Davis LC, Kress JW (1984) Practical cone-beam algorithm. *J Opt Soc Am A* 1:612–619
- Formaggia L, Lamponi D, Veneziani A (2006) Numerical modeling of 1D arterial networks coupled with a lumped parameters description of the heart. *Comput Methods Biomech Biomed Engin* 9(5):273–88
- Gan CT, Lankhaar JW, Westerhof N, Marcus JT, Becker A, Twisk JW, Boonstra A, Postmus PE, Vonk-Noordegraaf A (2007) Noninvasively assessed pulmonary artery stiffness predicts mortality in pulmonary arterial hypertension. *Chest* 132(6):1906–1912
- Guan D, Liang F, Gremaud PA (2016) Comparison of the Windkessel model and structured-tree model applied to prescribe outflow boundary conditions for a one-dimensional arterial tree model. *J Biomech* 49:1583–1592
- Hellmes HK, Haynes FW, Dexter L (1949) Pulmonary capillary pressure in man. *J Appl Physiol* 2(1):24–29
- Humphrey JD (2008) Mechanisms of arterial remodeling in hypertension: coupled roles of wall shear and intramural stress. *Hypertension* 52(2):195–200
- Hollander EH, Wang JJ, Dobson GM, Parker KH, Tyberg JV (2001) Negative wave reflections in pulmonary arteries. *Am J Physiol Heart Circ Physiol* 281(2):895–902
- Holzappel GA, Ogden RW (2010) Constitutive modelling of arteries. *Proc R Soc A* 466:1551–1597
- Hunter KS, Lammers SR, Shandas S (2011) Pulmonary vascular stiffness: measurement, modeling, and implications in normal and hypertensive pulmonary circulations. *Comput Physiol* 1:1413–1435
- Ioannou CV, Stergiopulos N, Katsamouris AN, Startchik I, Kalangos A, Licker MJ, Westerhof N, Morel DR (2003) Hemodynamics induced after acute reduction of proximal thoracic aorta compliance. *Eur J Vasc Endovasc Surg* 26:195–204
- Karau K, Johnson R, Molthen R, Dhyani A, Haworth S, Hanger C, Roerig D, Dawson C (2011) Microfocal X-ray CT imaging and pulmonary arterial distensibility in excised rat lungs. *Am J Physiol Heart Circ Physiol* 281:H1447–H1457
- Kheifets VO, O'Dell W, Smith T, Reilly JJ, Finol EA (2013) Considerations for numerical modeling of the pulmonary circulation—a review with a focus on pulmonary hypertension. *J Biomed Eng* 135:061011–2
- Krenz GS, Dawson CA (2003) Flow and pressure distributions in vascular networks consisting of distensible vessels. *Am J Physiol Heart Circ* 284(6):H2192–H2203
- Langewouters GJ, Wesseling KH, Goedhard WJ (1985) The pressure dependent dynamic elasticity of 35 thoracic and 16 abdominal human aortas in vitro described by a five component model. *J Biomech* 18:613–620
- Lee P, Carlson BE, Chesler N, Olufsen MS, Qureshi MU, Smith NP, Sochi T, Beard DA (2016) Heterogeneous mechanics of the mouse pulmonary arterial network. *Biomech Model Mechanobiol* 15:1245–1261
- Lankhaar JW, Westerhof N, Faes T, Marques K, Marcus J, Postmus P, Vonk-Noordegraaf A (2006) Quantification of right ventricular afterload in patients with and without pulmonary hypertension. *Am J Physiol Heart Circ Physiol* 29(4):H1731–173
- Li Y, Parker KH, Khir AW (2016) Using wave intensity analysis to determine local reflection coefficient in flexible tubes. *J Biomech* 49:2709–2717
- Lungu A, Wild JM, Capener D, Kiely DG, Swift AJ, Hose DR (2014) MRI model-based non-invasive differential diagnosis in pulmonary hypertension. *J Biomech* 47:2941–2947
- Lumens J, Delhaas T, Kirn B, Arts T (2009) Three-wall segment (TriSeg) model describing mechanics and hemodynamics of ventricular interaction. *Ann Biomed Eng* 37(11):2234–2255
- McDonald DA, Attinger EO (1965) The characteristics of arterial pulse wave propagation in the dog. *Inf Exchange Group No. 3, Sci Mem* 7

- Meaney JFM, Beddy P (2012) Pulmonary MRA. In: Carr J, Carroll T (eds) Magnetic resonance angiography. Springer, New York
- Mynard J, Penny DJ, Smolich JJ (2008) Wave intensity amplification and attenuation in non-linear flow: implications for the calculation of local reflection coefficients. *J Biomech* 41:3314–3321
- Mynard JP, Smolich JJ (2015) One-dimensional haemodynamic modeling and wave dynamics in the entire adult circulation. *Ann Biomed Eng* 43:144–1460
- Nichols WW, O'Rourke MF, Vlachopoulos C (2011) McDonald's blood flow in arteries: theoretical, experimental and clinical principles, 6th edn. Hodder Arnold, London
- Olufsen MS, Peskin CS, Kim WY, Pedersen EM, Nadim A, Larsen J (2000) Numerical simulation and experimental validation of blood flow in arteries with structured-tree outflow conditions. *Ann Biomed Eng* 28:1281–1299
- Olufsen MS, Hill NA, Vaughan GD, Sainsbury C, Johnson M (2012) Rarefaction and blood pressure in systemic and pulmonary arteries. *J Fluid Mech* 705:280–305
- Paun LM, Qureshi MU, Colebank M, Hill NA, Olufsen MS, Haider MA, Husmeier D (2018) MCMC methods for inference in a mathematical model of pulmonary circulation. *Stat Neerl* 1–33:2018
- Presson RG Jr, Audi SH, Hanger CC, Zenk GM, Sidner RA, Linehan JH, Wagner WW Jr, Dawson CA (1998) Anatomic distribution of pulmonary vascular compliance. *J Appl Physiol* 84(1):303–310
- Pursell ER, Vélez-Rendón D, Valdez-Jasso D (2016) Biaxial properties of the left and right pulmonary arteries in a monocrotaline rat animal model of pulmonary arterial hypertension. *ASME J Biomech Eng* 138:111004
- Qureshi MU, Vaughan GD, Sainsbury C, Johnson M, Peskin CS, Olufsen MS, Hill NA (2014) Numerical simulation of blood flow and pressure drop in the pulmonary arterial and venous circulation. *Biomech Model Mechanobiol* 13(5):1137–1154
- Qureshi MU, Hill NA (2015) A computational study of pressure wave reflections in the pulmonary arteries. *J Math Biol* 71:1525–1549
- Qureshi MU, Haider MA, Chesler NC, Olufsen MS (2017) Simulating the effects of hypoxia on pulmonary haemodynamics in mice. *Proc CMBE* 1:271–274
- Qureshi MU, Colebank MJ, Schreier DA, Tabima DM, Haider MA, Chesler NC, Olufsen MS (2018) Characteristic Impedance: frequency or time domain approach? *Physiol Meas* 39(1):014004. <https://doi.org/10.1088/1361-6579/aa9d60>
- Rasmussen CE, Williams CKI (2006) A computational study of pressure wave reflections in the pulmonary arteries. *J Math Biol* 71:1525–1549
- Reymond P, Merenda F, Perren F, Rufenacht D, Stergiopulos N (2009) Validation of a one-dimensional model of the systemic arterial tree. *Am J Physiol Heart Circ Physiol* 297:H208–H222
- Riches AC, Sharp JG, Thomas DB, Smith SV (1973) Blood volume determination in mouse. *J Physiol* 228(2):279–284
- Rich JD, Shah SJ, Swamy RS, Kamp A, Rich S (2011) Inaccuracy of Doppler echocardiographic estimates of pulmonary artery pressures in patients with pulmonary hypertension: implications for clinical practice. *Chest* 139:988–993
- Safaei S, Bradley CP, Suresh V, Mithraratne K, Muller A, Ho H, Ladd D, Hellevik L, Omholt SW, Chase JG, Miller LO, Watanabe SM, Blanco PJ, de Bono B, Hunter PJ (2016) Roadmap for cardiovascular circulation model. *J Physiol* 594(23):6909–6928
- Schreier DA, Hacker T, Hunder KS, Eickoff J, Liu A, Song G, Chesler NC (2014) Impact of hematocrit on right ventricular afterload during the progression of hypoxic pulmonary hypertension. *J Appl Physiol* 117(8):833–839
- Schwarz G (1978) Estimating the dimension of a model. *Ann Stat* 6:461–464
- Segers P, Rietzschel ER, De Buyzere ML, Vermeersch SJ, DeBacquer D, Van Bortel LM, De Backer G, Gillebert TC, Verdonck PR (2007) Noninvasive (input) impedance, pulse wave velocity, and wave reflection in healthy middle-aged men and women. *Hypertension* 49:1248–1255
- Simonneau G, Gatzoulis MA, Adatia I, Celermajer D, Denton C, Ghofrani A, Sanchez MA, Kumar RK, Landzberg M, Machado RF, Olschewski H, Robbins IM, Souza R (2013) Updated clinical classification of pulmonary hypertension. *J Am Coll Cardiol* 62:D34–D41
- Stergiopulos N, Meister JJ, Westerhof N (1995) Evaluation of methods for estimation of total arterial compliance. *Am J Physiol* 268:H1540–1548
- Tabima DM, Roldan-Alzate A, Wang Z, Hacker TA, Molthen RC, Chesler NC (2012) Persistent vascular collagen accumulation alters hemodynamic recovery from chronic hypoxia. *J Biomech* 45:799–804
- Tang B, Pickard S, Chan F, Tsao P, Taylor C, Feinstein J (2012) Wall shear stress is decreased in the pulmonary arteries of patients with pulmonary arterial hypertension: an image-based, computational fluid dynamics study. *Pulm Circ* 2(4):470–476
- Tran JS, Schiavazzi DE, Ramachandra AB, Kahn AM, Marsden AL (2017) Automated tuning for parameter identification and uncertainty quantification in multi-scale coronary simulations. *Comput Fluids* 142:128–138
- Tuder RM, Marecki JC, Richter A, Fijalkowska I, Flores S (2007) Pathology of pulmonary hypertension. *Clin Chest Med* 28(1):23–27
- Tawhai MH, Clark AR, Burrowes KS (2011) Computational models of the pulmonary circulation: insights and the move towards clinically directed studies. *Pulm Circ* 1(2):224–238
- Vanderpool RR, Kim AR, Chesler NC (2011) Effects of acute Rho kinase inhibition on chronic hypoxia-induced changes in proximal and distal pulmonary arterial structure and function. *J Appl Physiol* 110:188–198
- Valdez-Jasso D, Bia D, Zcalo Y, Armentano RL, Haider MA, Olufsen MS (2011) Linear and nonlinear viscoelastic modeling of aorta and carotid pressure-area dynamics under in vivo and ex vivo conditions. *Ann Biomed Eng* 39:1438–1456
- Valdez-Jasso D (2010) Modeling and identification of vascular biomechanical properties in large arteries. PhD thesis, North Carolina State University, Raleigh, NC
- van de Vosse FN, Stergiopulos N (2011) Pulse wave propagation in the arterial tree. *Annu Rev Fluid Mech* 43:467–499
- Watanabe S (2010) Asymptotic equivalence of Bayes cross validation and widely applicable information criterion in singular learning theory. *J Mach Learn Res* 11:3571–3594
- Watanabe S (2013) A widely applicable bayesian information criterion. *J Mach Learn Res* 14:867–897
- Wang Z, Chesler NC (2011) Pulmonary vascular wall stiffness: an important contributor to the increased right ventricular afterload with pulmonary hypertension. *Pulm Circ* 1(2):212–223
- Westerhof N, Sipkema P, Van Den Bos GC, Elzinga G (1972) Forward and backward waves in the arterial system. *Cardvasc Res* 6:648–656
- Westerhof N, Lankhaar J, Westerhof B (2009) The arterial windkessel. *Med Biol Eng Comput* 47:131–141
- Williams ND, Wind-Willassen O, Wright AA, Program REU, Mehlsen J, Ottesen JT, Olufsen MS (2014) Patient specific modeling of head-up tilt. *Math Med Biol* 31:365–392
- Willemet M, Alastruey J (2015) Arterial pressure and flow wave analysis using time-domain 1-D hemodynamics. *Ann Biomed Eng* 43:190–206

- Windberger U, Bartholovitsch A, Plasenzotti R, Korak KJ, Heinze G (2003) Whole blood viscosity, plasma viscosity and erythrocyte aggregation in nine mammalian species: reference values and comparison of data. *Exp Physiol* 88:431–440
- Yang W, Feinstein J, Vignon-Clementel I (2016) Adaptive outflow boundary conditions improve post-operative predictions after repair of peripheral pulmonary artery stenosis. *Biomech Model Mechanobiol* 15(5):1345–1353
- Yushkevich PA, Piven J, Hazlett HC, Smith RG, Ho S, Gee JC, Gerig G (2006) User-guided 3D active contour segmentation of anatomical structures: significantly improved efficiency and reliability. *Neuroimage* 31:1116–1128. www.itksnap.org

Publisher's Note Springer Nature remains neutral with regard to jurisdictional claims in published maps and institutional affiliations.